Structural and Multidisciplinary Optimization (2026) 69:242
https://doi.org/10.1007/s00158-026-04442-3

RESEARCH PAPER

Reliability-based topology optimization considering stochastic porosity defects in additive manufacturing

Yoo-Seong Park[1] · **Omid Nejadseyfi**[1] · **Matthijs Langelaar**[1]

Received: 22 April 2026 / Revised: 15 September 2026 / Accepted: 5 October 2026
© The Author(s) 2026

Abstract
Recent advancements in metal additive manufacturing (AM) technologies have enabled the precise fabrication of complex designs, promoting integration between topology optimization and AM. However, AM processes like laser powder bed fusion (LPBF) inevitably lead to microstructural defects, including keyhole-induced porosity and lack of fusion porosity. These pores significantly degrade the mechanical strength of printed components. The complexity of the process leads to the generation of random and unpredictable pores, which can vary from part to part even if all process parameters and geometry remain the same. Thus, this study proposes a reliability-based topology optimization framework that incorporates the uncertainty arising from random porosity defects during the AM process in a computationally efficient way. In this study, the probability of pore formation is assumed to increase linearly with distance from the build plate, which serves as a proxy for temperature. Assuming that defects are induced exclusively by overheating, the likelihood of pore formation increases with the temperature rise during the build process. A Monte Carlo approach is used to account for the stochastic pore realizations. To avoid performing a separate FEA for each realization, analytical stress fields around pores are used to augment the stress field obtained from a single FEA per optimization iteration. Adjoint sensitivity analysis is then employed for efficient gradient evaluation. Through 2D numerical examples on regular Cartesian grids, this study demonstrates and evaluates the effectiveness of the proposed approach while accounting for process-dependent stochastic porosity.

Keywords Process-related uncertainty · Stress-constrained topology optimization · Reliability-based topology optimization · Additive manufacturing

1 Introduction

Topology optimization has been widely recognized as a powerful tool for design optimization. Despite its advantages, the resulting designs are often highly complex, making them difficult to manufacture using traditional production methods. With the rapid growth of AM technologies, it has become possible to more precisely fabricate complex designs. But the integration of topology optimization and AM has also introduced challenges. For instance, issues such as overhanging features, minimum length, and enclosed voids have emerged, which can hinder the manufacturability of optimized designs. To address these issues, notable contributions have already been proposed. However, within the context of topology optimization, designing while considering AM-induced porosity remains an underexplored area.

In this study, we specifically focus on metal AM. Pore formation in metal AM, as shown in Fig. 1, is not solely caused by a single factor but results from the complex interaction of multiple factors such as temperature history, geometric features, and process conditions. These pores can be categorized as keyhole-induced porosity, lack of fusion, and gas porosity, depending on their cause and shape (Kim and Moylan 2018). The process of LPBF is so complex that even if the same part is printed twice using the same settings, typically defects with different sizes and locations occur. However, if defects do occur, their impact on the mechanical performance of parts can be severe (Snow et al. 2020; Al-Maharma et al. 2020; Wang et al. 2022a). Even small pores can cause stress concentration, ultimately leading to failure under a single static load or fractures under repeated loading (Seifi et al.

Responsible Editor: Ramin Bostanabad.

✉ Yoo-Seong Park
Y.S.PARK@tudelft.nl

[1] Computational Design & Mechanics, Mechanical Engineering Faculty, Delft University of Technology, Mekelweg 2, 2628 CD Delft, The Netherlands

Published online: 07 November 2026

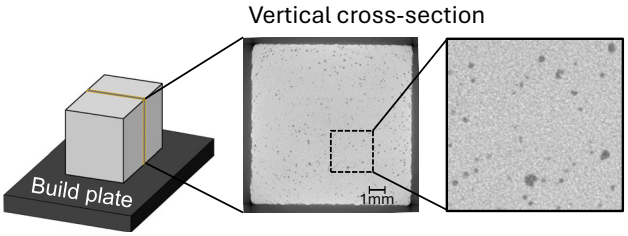


Fig. 1 Example of porosity defects in an LPBF-manufactured Ti-6Al-4V sample using micro-CT imaging: cross-sectional view

2017; Masuo et al. 2018). This highlights the importance of considering the probabilistic occurrence of pores in design, especially since they occur both inevitably and randomly during AM.

Uncertainty in the manufacturing process has been a growing concern in topology optimization research. To effectively consider uncertainty in topology optimization, three methods are typically used: RBTO, robust optimization, and worst-case scenario. RBTO employs stochastic constraints rather than deterministic ones, ensuring a target failure probability is satisfied. In contrast, a widely adopted approach in robust topology optimization is to formulate the objective as a weighted sum of the expectation and standard deviation. The worst-case scenario approach formulates the problem as a min-max optimization.

In 2009, the modeling of tolerance during manufacturing was incorporated into topology optimization by Sigmund (2009). Under/over etching of fabricated structures was modeled through image processing-based erosion and dilation operators. The robustness of the optimized design is ensured by applying the worst-case scenario. Wang et al. (2011) used a similar approach by enhancing it through the implementation of threshold projection. Schevenels et al. (2011) presented robust topology optimization considering spatially varying manufacturing errors. This study defined the threshold projection as a random variable. Similarly, it focuses on addressing under/over etching manufacturing errors. A key contribution is the consideration of spatially varying errors, rather than uniform errors, to better reflect realistic manufacturing errors. The problem was formulated using a robust optimization approach that minimizes both the mean and the standard deviation of the performance.

Jansen et al. (2013) addressed geometric imperfections. A density-based approach was adopted to simulate different types of geometric imperfections, focusing particularly on imperfections caused by material misplacement rather than surface errors. The robust optimization was formulated as a weighted sum of the mean compliance and its standard deviation. Keshavarzzadeh et al. (2017) presented both robust and reliability-based topology optimization considering geometric imperfections by applying the Heaviside thresholding approach. For more efficient implementation compared to sampling-based Monte Carlo simulation (MCS), Polynomial Chaos Expansion (PCE), a polynomial approximation technique, was proposed. Kriegesmann and Lüdeker (2019) focused on robust topology optimization using Taylor expansion approximation methods. This study considered three random variables, including geometry, to investigate and compare the accuracy of first- and second-order Taylor expansion-based uncertainty quantification methods. In the case of random geometry, the proposed First-Order Second Moment (FOSM) approach enabled a significant reduction in computational cost compared to MCS. da Silva et al. (2019) introduced stress-constrained topology optimization under manufacturing errors, building on the projection approach.

A recent study focused on reducing the part distortion occurring during AM (Komini et al. 2023). This paper defined the inherent strain leading to part distortion as an uncertain quantity in each layer, thus accounting for limitations of the modeling approach. A robust topology optimization formulation is applied to minimize its variation. Schmidt et al. (2024) proposed a robust topology optimization that considers the local friction coefficient of contact support as an uncertainty, which occurs as a form of manufacturing tolerance. These uncertainties are modeled as spatially correlated random fields, and Taylor expansion approximation-based FOSM was used for uncertainty quantification.

As mentioned earlier, many studies have employed topology optimization using probabilistic approaches to address uncertainties in manufacturing processes, primarily aiming to reduce variations from geometric imperfections. Recent trends have aimed at both improving the computational efficiency of robust topology optimization (Kriegesmann and Lüdeker 2019; Krüger and Kriegesmann 2024; Keshavarzzadeh et al. 2017; Mommeyer et al. 2024) and extending its applicability to cover a wider range of process-related uncertainties beyond geometry (Schmidt et al. 2024; Komini et al. 2023; Gu et al. 2026).

However, there has been limited research specifically focusing on uncertainties induced during AM. Certainly, a few studies have introduced topology optimization using probabilistic methods, considering local material properties under the process of AM (Keshavarzzadeh and James 2019; Greifenstein and Stingl 2020; Chen et al. 2026). However, these are closer to addressing the scatter in elastic modulus caused by unspecified reasons rather than directly accounting for the actual pore formation. The impact of stochastic pore formation and the resulting stress concentrations has received limited attention in topology optimization research. To fill this gap, this study proposes a reliability-based topology optimization framework that accounts for stochastic pore formation.

In this study, as our focus is on defining and exploring the probabilistic framework, for simplicity, the relation

between build height and temperature is assumed to be linear. As an additional assumption, this study considers pores induced by overheating, where higher temperatures lead to a higher likelihood of defect formation (King et al. 2014; Yavari et al. 2021; Mahtabi et al. 2023). The focus is placed on overheating-related defects, such as keyholing and gas porosity, while defects caused by insufficient energy, such as lack of fusion, are neglected.

Finally, as a first step in this line of work, the scope is restricted to 2D domains. Indeed, pore formation during AM is a complex phenomenon resulting from the interaction of factors such as transient thermal cycles and scan strategies. Because topology optimization relies on an iterative design update process, full-scale multiphysics modeling at every iteration becomes computationally prohibitive. To overcome this bottleneck, this study aims to narrow the gap through reasonable simplification. Rather than accurately capturing all physics, we focus on investigating how uncertainty in process-induced pores affects local stress constraints. Therefore, this simplified approach serves as a practical bridge between topology optimization for AM and AM-induced uncertainty.

The existence of a pore is probabilistically determined by a normalized random variable and a temperature-dependent pore probability variable. This approach conceptually incorporates both the randomness and the physics dependency of pore formation. The influence of pores on part quality is estimated in terms of local stress increase, where the stress concentration factor (SCF) approach is employed. We augment the stresses calculated by finite element analysis (FEA) using analytical stress fields around pores. As a result, a wide variety of pore-induced stress fields can be derived from a single FEA, making the approach computationally efficient. To address the resulting variation, reliability-based topology optimization with stress constraints is employed. Under AM process-induced uncertainty, the formulation incorporates probabilistic constraints using the reliability index to ensure an acceptable failure rate. For uncertainty quantification, MCS is employed. Since the SCF-based approach does not require additional FEA for each realization, MCS becomes computationally feasible.

The main contribution of this paper is a topology optimization framework that probabilistically accounts for AM-induced pores to achieve defect-tolerant designs. Since identical part quality cannot be guaranteed even under ideal process control, the aim is to model and quantify the uncertainty in pore formation to obtain a reliable design in the topology optimization scheme.

This paper is organized as follows: Sect. 2 introduces the modeling of random pore distribution based on the AM process. Section 3 presents the formulations of reliability-based and stress-based topology optimization. Section 4 provides numerical examples and discussion. Finally, the study is summarized and concluded in Sect. 5. Following the conclusion, Appendix A details the sensitivity analysis.

2 Probabilistic pore-field modeling in AM

2.1 Temperature-dependent pore prediction

Since the source of AM-induced porosity defects is limited to overheating in this study, the pore formation is assumed to depend on local temperature. At the same time, a key aspect of pore formation is its randomness. In other words, defects in the real world may still occur at lower temperatures with low probability, while high temperatures do not always lead to defects (Sanaei et al. 2019). Pores in AM are closely related to overheating, where the likelihood of defects increases beyond a specific temperature threshold (King et al. 2014; Yavari et al. 2021; Mahtabi et al. 2023). This phenomenon motivates the introduction of a temperature-dependent pore probability acting as a threshold, which will be elaborated in the following section. The overall procedure described in Sect. 2 is schematically summarized in Fig. 2.

To incorporate both this physics dependence and inherent randomness into the pore prediction, two variables are introduced. The first variable, x_i, is an auxiliary random variable, which takes values between 0 and 1. The second, p_i, is a pore probability dependent on the peak temperature at each scanning point during the AM process. In each element, x_i is sampled from a predefined probability distribution, such as a uniform distribution, as shown in Fig. 3. Here, the subscript i denotes the element number.

For the jth realization, the vector $\mathbf{X}^{(j)}$, containing all element random variables, is expressed as follows:

$$\mathbf{X}^{(j)} = \left\{ x_1^{(j)}, x_2^{(j)}, \ldots, x_n^{(j)} \right\}, \quad j = 1, 2, \ldots, N$$
$$\text{with } x_i^{(j)} \sim \mathcal{U}(0, 1), \quad \forall i = 1, 2, \ldots, n \tag{1}$$

where n denotes the number of elements and N is the total number of realizations. Each variable $x_i^{(j)}$ is independently sampled from a uniform distribution $\mathcal{U}(0, 1)$.

The pore indicator I_i is determined by comparing x_i to the pore probability p_i, as defined below:

$$I_i = \begin{cases} 0, & \text{if } x_i > p_i \quad \text{(no pore)} \\ 1, & \text{if } x_i \leq p_i \quad \text{(pore)} \end{cases} \tag{2}$$

Figure 3 illustrates the statistical occurrence of a pore within a single element. A histogram of 10^3 samples of x_i drawn from a uniform distribution is presented, along with the theoretical PDF shown as a black line. For example, with $p_i = 0.2$, samples in the red-shaded region correspond to

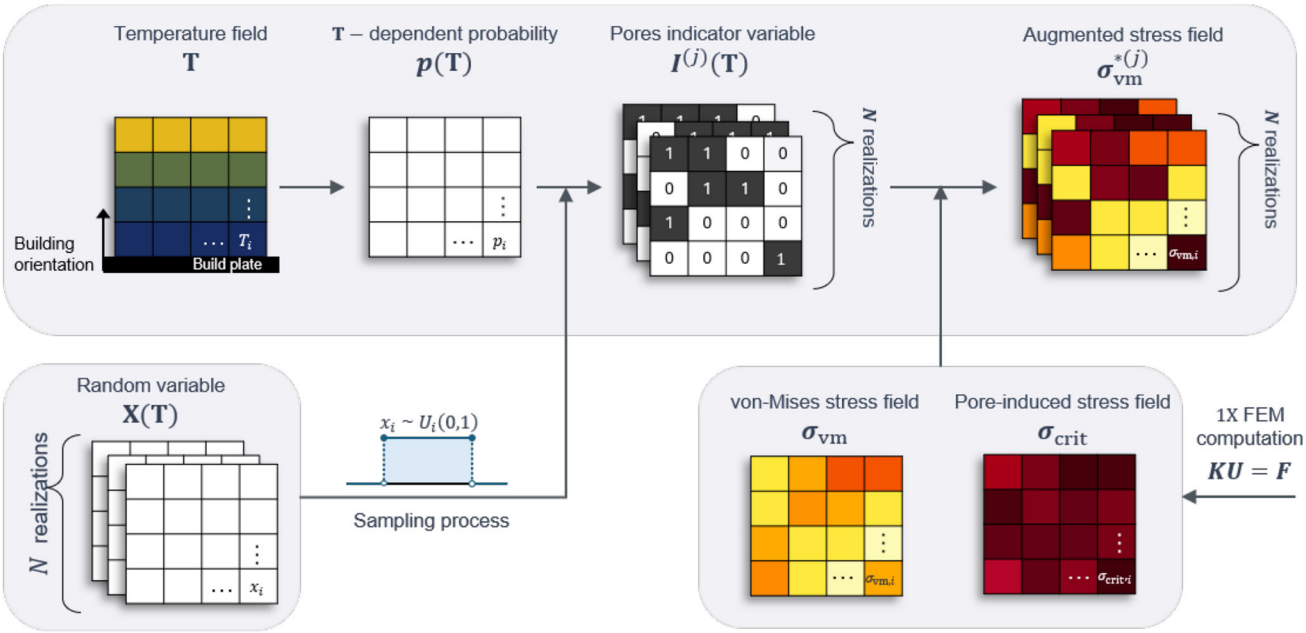


Fig. 2 Overall process for determining the stochastic augmented stress field. A temperature-dependent pore probability $\boldsymbol{p}(\mathbf{T})$ and random variables $\mathbf{X}(\mathbf{T})$ are introduced to create the pore indicator variables $\boldsymbol{I}(\mathbf{T})$, generating N distinct pore distribution scenarios. Consequently, N augmented stress fields are evaluated by integrating the nominal von Mises stress with the pore-induced local stress fields

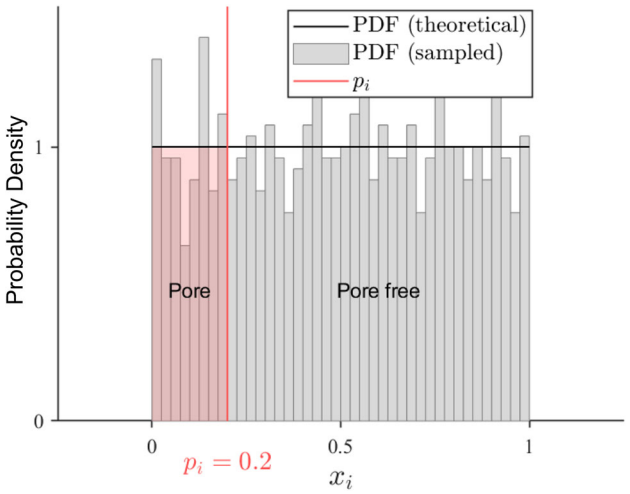


Fig. 3 Illustration of statistical pore formation with a histogram based on a uniform distribution

pore occurrence, while those in the remaining regions correspond to no pore.

The correlation between the local temperature T and the pore probability p_i is modeled using a linear expression, as shown in Eq. (3). An increase in temperature corresponds to an increase in p_i, implying a higher chance of pore formation. Let $p_{i,\min}$ and $p_{i,\max}$ denote the lower and upper bounds of p_i, and $T_{\min}$ and $T_{\max}$ be the corresponding bounds for T. Here, $T_{\min}$ is defined as the baseline temperature at the build plate, which corresponds to zero distance from the build plate. $T_{\max}$ is defined as the maximum temperature evaluated at the highest position within the design domain, representing the maximum distance from the build plate for a given part configuration. Accordingly, $p_i(T)$ can be expressed by normalizing the temperature within its physical bounds as follows:

$$p_i(T) = p_{i,\min} + (p_{i,\max} - p_{i,\min})\left(\frac{T - T_{\min}}{T_{\max} - T_{\min}}\right) \tag{3}$$

It should be noted that $p_i(T)$ applies to the reference mesh for each numerical example. As specified in Table 1, all lengths in this study are dimensionless, and each finite element has a unit edge length. The pore probability must be scaled according to the number of elements in the refined mesh. This ensures that the expected number of defects does not increase under mesh refinement. When the reference mesh is uniformly refined, the pore probability is scaled as follows:

$$p_i^{\text{scaled}}(T) = \frac{p_i(T)}{r_{\text{mesh}}}. \tag{4}$$

Here, $r_{\text{mesh}} = n/n_{\text{ref}}$ is the mesh refinement factor, where n and n_{ref} denote the numbers of elements in the refined and reference meshes, respectively.

The aim of this study is not to precisely predict the physical mechanisms of pore formation, as many studies (Wang et al. 2022b; Cook and Murphy 2020; Bayat et al. 2019) attempt to do, but to probabilistically model the presence of pores

Table 1 General settings for numerical examples

Description	Setting/value
Model	Plane stress
Element type	Bi-linear 4 node quadrilateral
Young's modulus	$E_0 = 1.0$
Poisson's ratio	$\nu = 0.3$
Filter radius	$r_{\min} = 3.0$

and incorporate it into a topology optimization framework for the first time. Certainly, temperature history is a complex function of scan speed, laser power, geometric complexity, and material properties (Gu et al. 2012; Diegel et al. 2020), which also involves the complex reheating effects within the deposited layers. Furthermore, a high concentration of pores typically occurs along geometric edges where the scanning laser changes direction (Leung et al. 2018). However, this study operates under the simplification that the temperature increases linearly with distance from the build plate, neglecting the transient reheating process. At this stage, we prioritize computational efficiency over physics-based precision, enabling integration with topology optimization. While this strategy sacrifices some physical fidelity in favor of computational tractability, it serves as a practical baseline that allows subsequent expansion toward more realistic physics.

2.2 Stress evaluation using SCF for AM-induced pores

For clarity in evaluating AM-induced pores, we base our assumptions on relevant research. A few studies have estimated the stress concentration caused by porosity defects in AM-manufactured components using finite element analysis (Biswal et al. 2018; Afroz et al. 2024). These studies provide a detailed investigation into the characteristics of pores and their quantitative correlation with the stress concentration factor (SCF). Based on these prior studies, we make several assumptions about pore characteristics.

1. **Circular pore representation** Pores caused by overheating at excessively high energy density are typically spherical (Galarraga et al. 2016) and are modeled in this work as circular holes in a two-dimensional (2D) domain. Therefore, the influence of defect shape (e.g., elongated or irregular shapes) on the SCF is neglected in this study.
2. **Internal pores only** In practice, pores can be classified as internal or sub-surface depending on their location. It is known that as a pore approaches the free surface, its SCF increases substantially. Considering sub-surface effects in pore prediction is beyond the scope of this study.
3. **Negligible size effect** For internal pores, the influence of pore size on the SCF is not considered dominant when the pore size is below a certain threshold. The focus of this study is on microscale pores whose dimensions are small relative to those of the AM-produced part. The variation in the SCF with respect to size can be assumed to be insignificant.
4. **No interaction between pores** Each pore is treated as an isolated hole in an infinite plane. Potential interactions between multiple pores, which could further increase the SCF, are neglected.
5. **Centroid placement** Pores are positioned at element centers with sizes much smaller than element dimensions, modeled as holes in infinite planes (Fig. 4).

In addition, the proposed model focuses on local stress amplification and neglects the pore-induced reduction in effective stiffness. This is justified by the scale difference between the pore and the finite element. However, if the mesh is refined to an extreme resolution where the pore size becomes comparable to the element size, incorporating the stiffness reduction would become necessary.

While FEA enables direct calculation of stress concentration by accounting for geometric features, it is computationally expensive. Given numerous pore-field realizations from the proposed stochastic method in Sect. 2.1, the computational effort required for calculating reliability can be substantial. Thus, this section describes the use of analytical stress fields around the pores to augment the stress fields obtained from FEA on a domain without including pores. This approach aims to provide an efficient way to calculate reliability and incorporate pore effects into stress-constrained topology optimization.

The occurrence of porosity defects results in a modification of the stress state. This localization of high stress is known as stress concentration and is measured by the SCF. Since the scope of this work is limited to a 2D domain, we adopt a 2D plane stress condition where a pore is modeled as a circular hole. For an infinite 2D plane under uniaxial tension, it is well established that the SCF reaches a value of three (Pilkey et al. 2020; Kirsch 1898). This well-known factor-of-three arises from Kirsch's solution for the hoop stress at the hole. At the edge of the hole, where radial and shear stresses are zero due to the free surface, the hoop stress is given by

$$\sigma_{\theta\theta} = \sigma_{\infty}(1 - 2\cos 2\theta). \tag{5}$$

When $\theta = 0$ is aligned with the remote loading, the maximum stress occurs at $\theta = \pm 90°$, reaching three times the applied stress.

The factor-of-three is only valid where the far-field stress is uniaxial. For a general loading condition, the SCF formulation needs to be extended to a general 2D loading. By applying the principle of linear superposition of two uniaxial and a shear load (Kirsch 1898), the analytical solution can

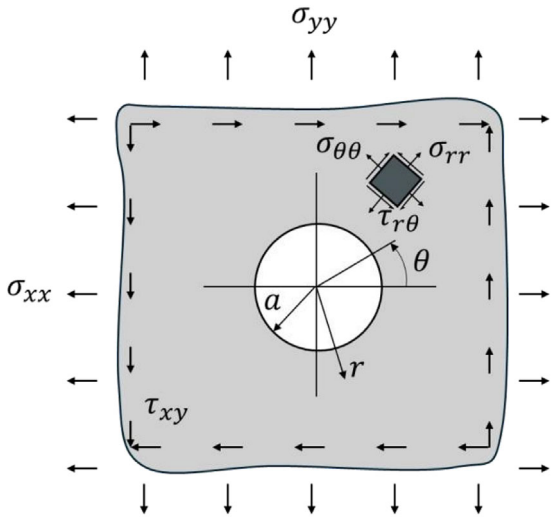


Fig. 4 Schematic representation of stress state around holes in a 2D infinite plane for general loading. a: hole radius, r: radial coordinate, $\theta = 0$ is aligned with σ_{xx}

be expressed as follows (see Fig. 4 as a schematic illustration for stress state):

$$\begin{aligned}
\sigma_{rr} &= \tfrac{\sigma_{xx}+\sigma_{yy}}{2}\left(1-\left(\tfrac{a}{r}\right)^2\right) \\
&\quad + \left(1-4\left(\tfrac{a}{r}\right)^2+3\left(\tfrac{a}{r}\right)^4\right) \\
&\quad \times \left(\tfrac{\sigma_{xx}-\sigma_{yy}}{2}\cos 2\theta + \tau_{xy}\sin 2\theta\right), \\
\sigma_{\theta\theta} &= \tfrac{\sigma_{xx}+\sigma_{yy}}{2}\left(1+\left(\tfrac{a}{r}\right)^2\right) \\
&\quad - \left(1+3\left(\tfrac{a}{r}\right)^4\right) \\
&\quad \times \left(\tfrac{\sigma_{xx}-\sigma_{yy}}{2}\cos 2\theta + \tau_{xy}\sin 2\theta\right), \\
\tau_{r\theta} &= \left(1+2\left(\tfrac{a}{r}\right)^2-3\left(\tfrac{a}{r}\right)^4\right) \\
&\quad \times \left(\tfrac{\sigma_{yy}-\sigma_{xx}}{2}\sin 2\theta + \tau_{xy}\cos 2\theta\right).
\end{aligned} \tag{6}$$

At the hole's edge, the hoop stress is given by,

$$\begin{aligned}
\sigma_{\theta\theta}\big|_{r=a} &= (\sigma_{xx}+\sigma_{yy}) \\
&\quad - 2(\sigma_{xx}-\sigma_{yy})\cos 2\theta - 4\tau_{xy}\sin 2\theta.
\end{aligned} \tag{7}$$

It is noted that $\sigma_{\theta\theta}$ is the only non-zero stress component at the hole due to the free surface condition. This is a special case ($a = r$) where the maximum stress equals the von Mises stress. The maximum value, obtained by differentiation, is given as follows:

$$\sigma_{\theta\theta}^{\max} = (\sigma_{xx}+\sigma_{yy}) + 2\sqrt{(\sigma_{xx}-\sigma_{yy})^2+4\tau_{xy}^2}, \tag{8}$$

Because of the periodicity of the trigonometric functions, multiple angular points satisfy the maximum condition. The solution is expressed as:

$$\theta_{\max} = \tfrac{1}{2}\tan^{-1}\left(\frac{2\tau_{xy}}{\sigma_{xx}-\sigma_{yy}}\right) + \frac{k\pi}{2}, \quad k \in \mathbb{Z}. \tag{9}$$

This solution, Eq. (8), is divided by the reference stress (e.g., von Mises stress) and used as SCF under general 2D loading conditions. If the reference stress without a hole, denoted as σ_{ref}, is used, K_t at the hole is expressed as:

$$K_t = \frac{\sigma_{\theta\theta}^{\max}}{\sigma_{\text{ref}}} \tag{10}$$

In this study, only tensile stress amplification is treated as detrimental, while pore-induced amplification under predominantly compressive states is neglected (Nayebi et al. 2021; Rice and Tracey 1969; Kan et al. 2022). In certain cases, the stress states do not contribute to stress concentration around the hole but rather have a beneficial effect. This unexpected stress-reducing effect is neglected in this study. Thus, a smooth-maximum operator $\mathcal{S}_\varepsilon$ is introduced to enforce a lower bound on $\sigma_{\theta\theta}^{\max}$. Specifically, $\sigma_{\theta\theta}^{\max}$ is redefined as the critical stress $\sigma_{\text{crit}} = \mathcal{S}_\varepsilon(\sigma_{\theta\theta}^{\max}, \sigma_{\text{ref}})$, ensuring that K_t is not applied to compressive stresses.

$$\begin{aligned}
\sigma_{\text{crit}} &= \mathcal{S}_\varepsilon(\sigma_{\theta\theta}^{\max}, \sigma_{\text{ref}}) \\
&= \frac{1}{2}\left(\sigma_{\theta\theta}^{\max}+\sigma_{\text{ref}}\right) + \frac{1}{2}\sqrt{\left(\sigma_{\theta\theta}^{\max}-\sigma_{\text{ref}}\right)^2+\varepsilon},
\end{aligned} \tag{11}$$

where ε is a parameter controlling the smoothness of the approximation (set to 10^{-10} in this study).

To extend this SCF-based approach to a 3D problem, the augmented stress can be computed by employing the analytical solution for a 3D stress state (Davis et al. 2017; Jaeger et al. 2009). By transforming a remote 3D stress tensor into its principal components, the stress field around a 3D void can be readily evaluated using these analytical solutions and the principle of superposition. While the current 2D restriction is adopted as a baseline to validate the framework without initial modeling complications, this underlying formulation can be conceptually extended to 3D problems, despite the increased numerical expense of 3D FE analysis and Monte Carlo simulations.

3 Topology optimization

AM-induced porosity increases local stress and thereby affects the performance requirements of the optimal design. To account for this effect, the SCF derived in the previous section is incorporated into a stress-constrained topology optimization, as discussed in Sect. 3.1.

In addition, the SCF-based approach includes different defect scenarios, which are regarded as uncertainties,

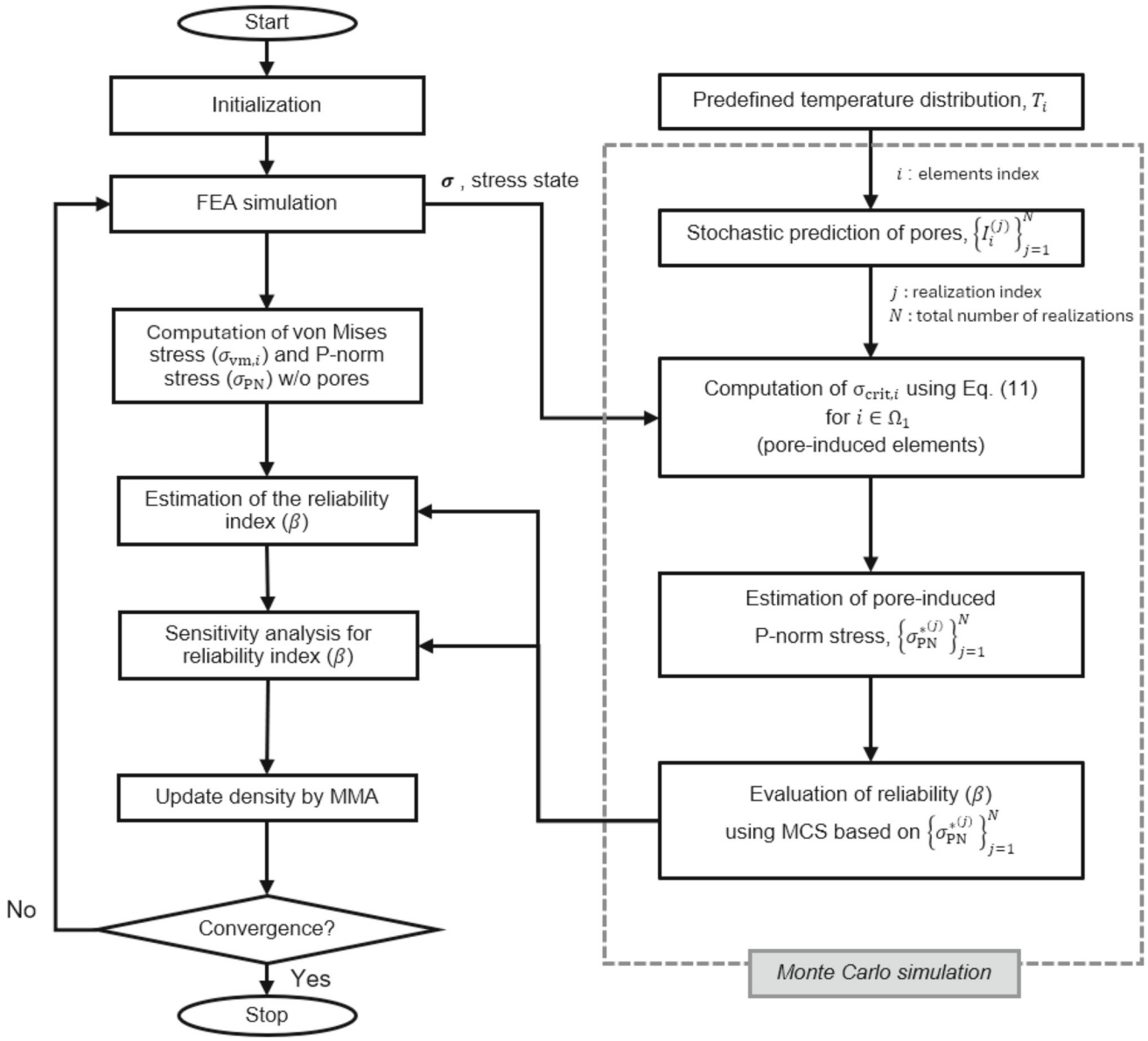


Fig. 5 Illustration of the flow chart for the proposed RBTO framework considering AM-induced pores

and this may lead to violations of the stress constraint in the deterministic formulation. To address this uncertainty, a reliability-based topology optimization is integrated in Sect. 3.2. To better explain the proposed RBTO framework, the complete flowchart of the algorithm is illustrated in Fig. 5.

3.1 Stress-constrained topology optimization

In this study, density-based topology optimization is employed assuming linear elastic material behavior. The density design variable ρ_i at each element is constrained between 0 and 1, representing void and solid material, respectively. We adopt the modified SIMP model (Sigmund 2007) to define the material properties as:

$$E_e(\rho_i) = E_{\min} + \eta_c(\rho_i)(E_0 - E_{\min}) \tag{12}$$

where $E_e(\rho_i)$ denotes the effective Young's modulus of element i and E_0 is the Young's modulus of the solid material. To avoid singularity of the global stiffness matrix, a small value $E_{\min} = 10^{-9}E_0$ is defined for the void density. For the stiffness penalization, an interpolation function, $\eta_c(\rho_i) = (\rho_i)^p$, is introduced. The parameter for penalization is set to the common value of $p = 3$ to achieve a black-and-white design by penalizing intermediate densities. In addition, the density filtering scheme is used to ensure mesh-independence and to avoid the checkerboard issue (Bruns and Tortorelli 2001).

In topology optimization with local stress constraints, two well-known challenges arise: (1) singular optima and (2) the local nature of stress constraints. First, a singular optimum is a local optimum that is inaccessible by gradient-based optimizers. This is an unavoidable problem when using density-based topology optimization. To deal with this fundamental challenge, one commonly used approach is the relaxation or penalization method (Bruggi and Duysinx 2012; Le et al. 2010; Holmberg et al. 2013). In this work, we use the relaxation scheme suggested by Le et al. (2010). The relaxed stress vector, $\hat{\boldsymbol{\sigma}}_i$ for an element is expressed as follows:

$$\begin{aligned} \hat{\boldsymbol{\sigma}}_i &= \eta_s(\rho_i)\boldsymbol{\sigma}_i \\ \eta_s(\rho_i) &= (\rho_i)^q \end{aligned} \tag{13}$$

Here, the interpolation function $\eta_s(\rho_i)$ is used to penalize intermediate design variables. In this study, a relaxation approach with $q = \frac{1}{3}$ is employed. The elemental stress vector $\boldsymbol{\sigma}_i$ is defined by the constitutive matrix $\mathbf{D}$ based on the non-penalized Young's modulus, the strain–displacement matrix $\mathbf{B}_i$ and the local displacement $\mathbf{u}_i$ at each element as follows:

$$\boldsymbol{\sigma}_i = \mathbf{D}\mathbf{B}_i\mathbf{u}_i \tag{14}$$

Another challenge in stress-based topology optimization is the large number of constraints. Due to the local nature of stress values, the number of constraints typically equals the number of design variables. From a computational perspective, a more practical approach is needed to obtain a global stress measure. To formulate a global stress measure while ensuring differentiability, P-norm or Kreisselmeier–Steinhauser (KS) functions can be employed (Yang and Chen 1996; Le et al. 2010; Duysinx and Sigmund 1998). In this study, the standard P-norm approach is used, and the global stress measure is given as follows:

$$\sigma_{\text{PN}} = \left(\sum_{i=1}^{n} (\sigma_{\text{vm},i})^P \right)^{1/P}, \tag{15}$$

where P is the stress norm parameter and n is the number of elements. $\sigma_{\text{vm},i}$ is the equivalent stress or von Mises stress value on each element derived from $\hat{\boldsymbol{\sigma}}_i$. The definition of von Mises stress at each element for two dimensions is expressed by

$$\sigma_{\text{vm},i} = (\sigma_{ix}^2 + \sigma_{iy}^2 - \sigma_{ix}\sigma_{iy} + 3\tau_{ixy}^2)^{\frac{1}{2}}. \tag{16}$$

Moreover, an adaptive scaling approach is applied to provide more physical meaning to the approximated stress value during optimization (Le et al. 2010). It is noted that rescaling is not applied at every iteration but rather every 20 iterations to maintain the continuity of sensitivity.

The scaled P-norm stress, $\hat{\sigma}_{\text{PN}}$, is defined using a scaling coefficient c that is updated at every k iteration as follows:

$$\begin{aligned} \hat{\sigma}_{\text{PN}} &= c\,\sigma_{\text{PN}}, \\ c^k &= \zeta \frac{\sigma_{\max}^{(k-1)}}{\sigma_{\text{PN}}^{(k-1)}}, \end{aligned} \tag{17}$$

$\sigma_{\max}^{(k-1)}$ denotes the maximum von Mises stress, and $\sigma_{\text{PN}}^{(k-1)}$ is the P-norm stress measure that is obtained from the previous iteration. A relaxation factor $0 < \zeta \leq 1$ is applied to improve the numerical stability.

Accordingly, the deterministic stress-based topology optimization with a global stress measure approach is formulated as follows:

$$\begin{aligned} &\min_{\boldsymbol{\rho}} V(\boldsymbol{\rho}) = \frac{1}{V_0} \sum_{i=1}^{n} v_i \rho_i \\ &\text{s.t.} \quad \mathbf{K}(\boldsymbol{\rho})\mathbf{U}(\boldsymbol{\rho}) = \mathbf{F} \\ &\qquad 0 \leq \rho_i \leq 1 \quad (i = 1, 2, ..., n) \\ &\qquad \frac{c\,\sigma_{\text{PN}}}{\bar{\sigma}_{\text{a}}} - 1 \leq 0 \end{aligned} \tag{18}$$

where ρ_i represents the density design variable in each element, which is bounded between 0 and 1. V is the volume fraction of the structure that is a function of design variable $\boldsymbol{\rho}$; v_i is the volume of each element; V_0 is the volume of the entire design domain; and n denotes the number of elements.

$\mathbf{K}$ is the global stiffness matrix, $\mathbf{U}$ is the global displacement vector, $\mathbf{F}$ is the global load vector and $\bar{\sigma}_{\text{a}}$ denotes the allowable stress. To account for the influence of pores, a modified von Mises stress is evaluated. Using the defect indicator I_i introduced in Eq. (2), the affected elements are identified. For these elements, the amplified stress is expressed as σ_{crit}. Accordingly, the augmented stress measure at the element level, $\sigma_{\text{vm},i}^*$, is defined as follows:

$$\sigma_{\text{vm},i}^* = \begin{cases} \sigma_{\text{vm},i}, & i \in \Omega_0 \\ \sigma_{\text{crit},i}, & i \in \Omega_1 \end{cases}, \quad (i = 1, \ldots, n) \tag{19}$$

Here, let Ω_0 and Ω_1 denote the sets of elements without and with pores. When a pore is present within an element, instead of $\sigma_{\text{vm},i}$, we use the modified $\sigma_{\text{crit},i}$, obtained by Eq. (11).

Incorporating the effect of pores, $\sigma_{\mathrm{vm},i}$ in Eq. (15) is replaced with $\sigma^*_{\mathrm{vm},i}$. Accordingly, the P-norm stress is expressed as σ^*_{PN} as follows:

$$\sigma^*_{\mathrm{PN}} = \left(\sum_{i=1}^{n} (\sigma^*_{\mathrm{vm},i})^P \right)^{1/P}, \tag{20}$$

Finally, the stress constraint in Eq. (18) is reformulated using σ^*_{PN} as given below.

$$\frac{c\,\sigma^*_{\mathrm{PN}}}{\bar{\sigma}_{\mathrm{a}}} - 1 \leq 0 \tag{21}$$

3.2 Reliability-based topology optimization

Although deterministic topology optimization (DTO) is a powerful tool for structural design, its outcomes are optimized for ideal conditions. Real-world uncertainties, such as variations in material properties and loading conditions, and manufacturing tolerances, may lead to constraint violations. Consequently, DTO alone has limitations in ensuring structural reliability. The worst-case method can also be implemented to optimize for the most unfavorable pore distribution, but such an approach necessarily results in an overly conservative solution. Therefore, in the RBTO formulation, conventional deterministic constraints are converted into probabilistic ones to control the failure rate.

In this study, the pore-induced constraint defined in Eq. (21) is reformulated for the design of defect-tolerant AM parts. This accounts for variations in σ^*_{PN} introduced by the random variable in Eq. (1). We use a probabilistic stress constraint with a limit state function, $G(\boldsymbol{\rho}, \mathbf{X})$. When $\mathbf{X} \in \mathbb{R}^n$ is a vector containing random variables in the problem, $G(\boldsymbol{\rho}, \mathbf{X})$ is the limit-state function used to determine whether the aggregated stress measure exceeds the allowable stress, defined as:

$$G(\boldsymbol{\rho}, \mathbf{X}) = \bar{\sigma}_a - c\,\sigma^*_{\mathrm{PN}}(\boldsymbol{\rho}, \mathbf{X}) \tag{22}$$

Here, the scaling coefficient c is used in the same manner as in DTO (Eq. (21)).

With P_r representing the probability of a particular event, Eq. (22) is reformulated by using limit state function $G(\boldsymbol{\rho}, \mathbf{X})$ as follows:

$$P_f = P_r[G(\boldsymbol{\rho}, \mathbf{X}) < 0] \leq P_t \tag{23}$$

where P_f denotes the failure probability, and P_t is the target failure probability defined by design requirements.

In general, Eq. (23) cannot be obtained analytically, as it involves the joint probability density function, which is often unknown. Therefore, practical approaches rely on sampling techniques, surrogate-based approaches (Nejadseyfi et al. 2019), or Taylor expansion based approximation methods such as First-Order Reliability Method (FORM), and Second-Order Reliability Method (SORM) (Tu et al. 1999). In this study, we employ the MCS approach to estimate the statistical moments of the limit-state function and evaluate the failure probability through the corresponding reliability index. Even though MCS is generally costly, it becomes feasible in our case because the SCF-based approach does not require additional FEA. Thus, the computational effort of MCS remains acceptable.

The MMA algorithm (Svanberg 1987) is used to solve the optimization problem and the derivative of the constraint with respect to the design variables is required. Therefore, the probabilistic constraint is reformulated in terms of the safety index or reliability index, β. Especially, when $G(\boldsymbol{\rho}, \mathbf{X})$ follows a normal distribution, the original random space is transformed into standard normal space. Consequently, the reliability index β is defined as a ratio of the mean to the standard deviation of the limit state function as follows:

$$P_r[G(\boldsymbol{\rho}, \mathbf{X}) < 0] = \Phi(-\beta), \quad \text{where} \quad \beta = \frac{\mu_G}{\sigma_G} \tag{24}$$

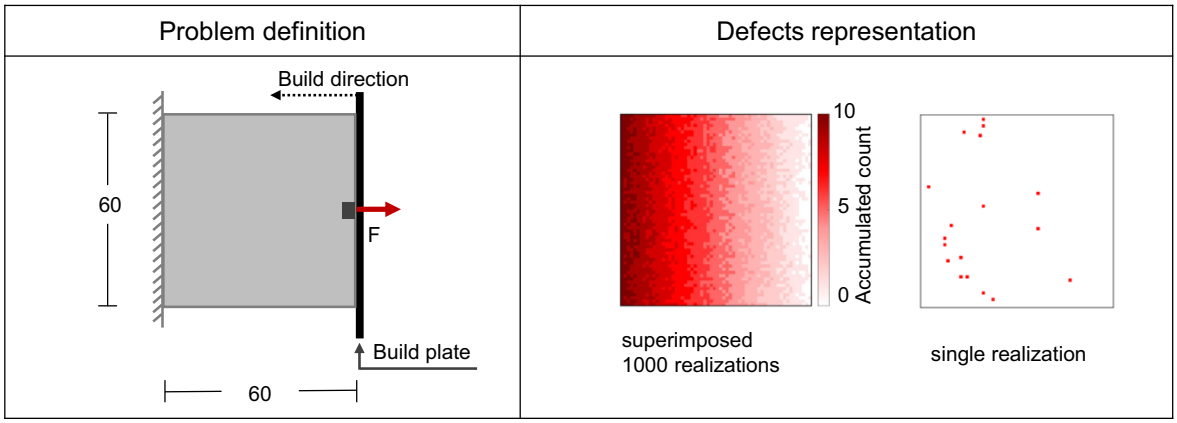
where $\Phi(\cdot)$ denotes the cumulative distribution function of the standard normal distribution. Ultimately, the formulation for RBTO with stress constraints becomes:

$$\begin{aligned} \min_{\boldsymbol{\rho}} \quad & V(\boldsymbol{\rho}) \\ \text{s.t.} \quad & \mathbf{K}(\boldsymbol{\rho})\mathbf{U}(\boldsymbol{\rho}) = \mathbf{F} \\ & 0 \leq \rho_i \leq 1 \\ & P_f = P_r[G(\boldsymbol{\rho}, \mathbf{X}) < 0] \leq P_t \\ & \Leftrightarrow \quad g(\boldsymbol{\rho}, \mathbf{X}) = 1 - \frac{\beta}{\beta_t} \leq 0 \end{aligned} \tag{25}$$

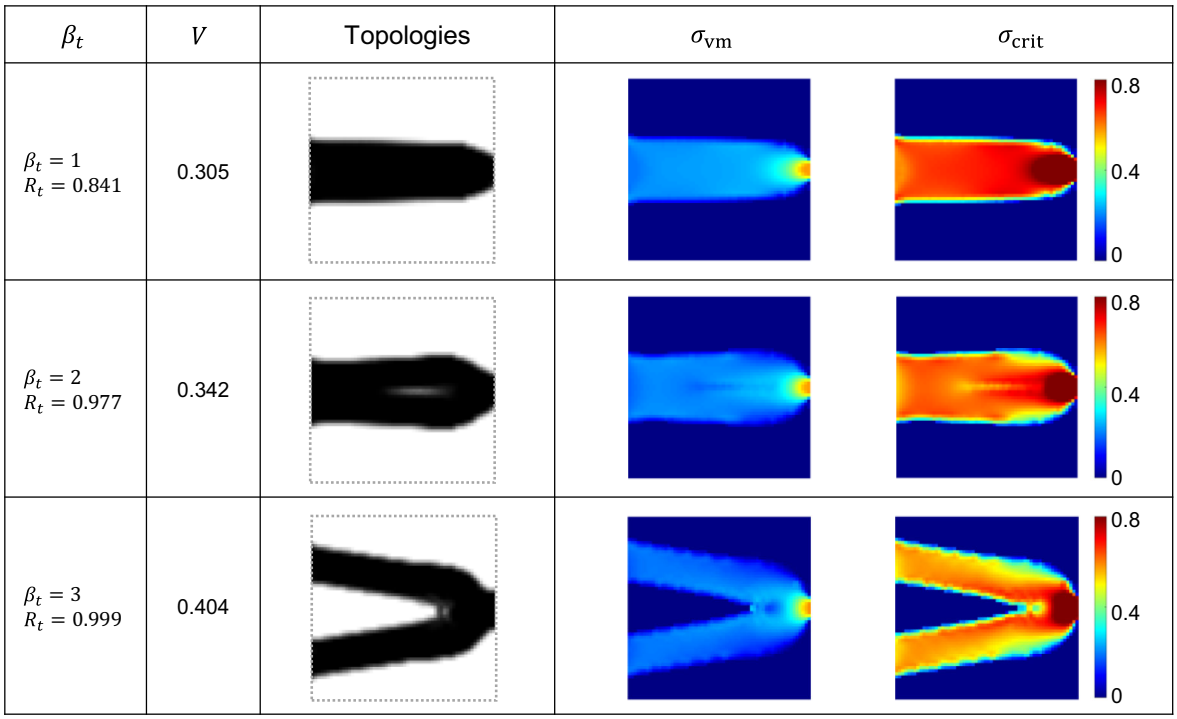
where β_t denotes the target reliability index corresponding to the target failure probability P_t.

4 Numerical examples

In the numerical examples section, three benchmark problems are presented: the fixed wall tensile bar, half MBB beam, and L-bracket. The general problem settings are summarized in Table 1. For generality, all numerical examples are treated as dimensionless. The structure has a unit thickness and every element has a unit edge length. The Method of Moving Asymptotes (MMA) algorithm is applied with its default parameters (Svanberg 1987), except for a reduced move limit of 0.01. Stress constraints are aggregated via a P-norm with $P = 12$. In all numerical examples except for the first tension bar example, the optimization was initialized with a solid design domain where all element densities



(a)



(b)

Fig. 6 Tensile bar: **a** problem definition and pore representation; **b** optimized design and stress distribution using RBTO. All the stress fields are scaled to [0, 0.8], consistent with the allowable stress ($\bar{\sigma}_{\text{a}} = 0.8$)

were set to $\boldsymbol{\rho} = \mathbf{1}$. For the tension bar example, the central half of the domain height was initialized as a horizontal solid bar $\boldsymbol{\rho} = \mathbf{1}$ extending the full domain length, with void elsewhere. This initialization was chosen to mitigate convergence to unfavorable local minima encountered with a fully solid initial design. Regarding the convergence behavior, the maximum change in density is set below 10^{-4} for both DTO and RBTO. For the implementation details of the optimization, the set of generated random samples is fixed throughout the optimization process to ensure stable convergence. Furthermore, Latin Hypercube Sampling is employed to obtain well-distributed random samples.

4.1 Example 1: fixed wall tensile bar

A fixed wall tensile bar problem is considered, as depicted in Fig. 6a. The design domain is meshed with 3600 (60×60) bilinear quadrilateral elements. A load of magnitude $F = 4$

Table 2 Parameters for the temperature-dependent probabilistic pore model

Parameter	Value	Description
$p_{i,\min}$	10^{-4}	Minimum pore probability
$p_{i,\max}$	10^{-2}	Maximum pore probability
$T_{\min}$	200	Minimum temperature [°C]
$T_{\max}$	1000	Maximum temperature [°C]

is distributed over 7 nodes. To avoid stress concentration near the loaded region, a 6×4 element patch (filled with dark gray) is treated as a non-design area maintained at full density throughout optimization. The allowable stress $\bar{\sigma}_a$ is set to 0.8.

4.1.1 Reliability-based vs. safety factor TO

As illustrated in Fig. 2, a probabilistic pore-field is applied under the assumption that pore formation depends linearly on temperature. For this problem, temperature increases from right to left across the design domain, assuming that this is the printing orientation. The parameters related to Eq. (3) are summarized in Table 2, and these values are consistently applied throughout all three numerical examples. Specifically, $p_{i,\min} = 10^{-4}$ and $p_{i,\max} = 10^{-2}$, meaning a 0.01% probability of pore occurrence at the right-side layer and a 1% probability at the left-side during fabrication. Depending on the probability of pore occurrence, the spatial distribution of pores varies across different sampling realizations.

To visualize the pore distribution, Fig. 6a displays 10^3 superimposed realizations used in the optimization, which effectively illustrate the overall statistical distribution. Alongside these superimposed images, a single representative realization is also presented to provide a clear view of an individual instance.

In Fig. 6b, optimized topologies for various β_t values are shown with von Mises stress σ_{vm} and critical stress σ_{crit}. During optimization, each stress map emerges from spatially varying pore distributions across realizations, forming augmented stress fields with unique combinations of σ_{vm} and σ_{crit} (see Fig. 7 as an example). Because 10^3 distinct mappings are generated, presenting every stress distribution is impractical. Consequently, to maintain visual clarity, we present only these two stress cases, σ_{vm} and σ_{crit} in the following numerical examples.

Regarding the optimal designs, three cases with different β_t values are presented. The target reliability index β_t values range from 1 to 3, representing target reliability $R_t = 0.841, 0.977$, and 0.999, respectively. The first notable observation is that volume increases with higher reliability index. Material is added to critical regions near the load area, yielding distinct topologies at the three reliability levels. A

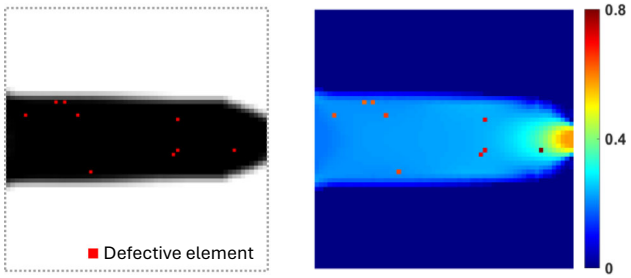


Fig. 7 Tensile bar: Actual stress mapping for one specific pore realization using RBTO ($\beta_t = 1$). Left: optimized density with pores (red fill indicates defective elements). Right: an augmented stress field considering pore-induced stress magnitude

Design (SF)	V	Topologies
DTO (SF = 1)	0.107	
DTO (SF = 1.5)	0.177	
DTO (SF = 2)	0.333	

Fig. 8 Tensile bar: optimized design using DTO with different safety factors (SF = 1, 1.5 and 2)

notable topology change with increasing β_t is the splitting of the tension bar, which helps distribute the stress concentration near the load area. This behavior is also observed in the DTO designs (Fig. 8) obtained with different safety factors (SF), as will be discussed below.

Applying SF is a common methodology in structural engineering to ensure reliability, where the allowable stress is divided by the SF value. In this example, SF = 1.5 and SF = 2

Table 3 Tensile bar: reliability verification via 10^5 realizations for RBTO and SF-based designs

Method	Target	β	P_f	δ_β (%)
RBTO	$\beta_t = 1$	1.053	0.1462	+5.3
	$\beta_t = 2$	2.093	0.0182	+4.7
	$\beta_t = 3$	3.181	0.0007	+6.0
Safety factor	SF = 1	−2.298	0.9892	–
	SF = 1.5	−1.667	0.9505	–
	SF = 2	0.881	0.1891	–

A negative reliability index (β) indicates that the probability of failure exceeds 0.5, meaning that failure occurs in more than half of the realizations

yield allowable stresses of 0.533 and 0.4, respectively, resulting in increased material volumes.

Reliability indices under defect uncertainty are reported in Table 3, verified using 10^5 realizations. To evaluate the verification accuracy against the target reliability, the relative deviation is defined as $\delta_\beta = (\beta - \beta_t)/\beta_t \times 100\%$. The RBTO method closely satisfies the target constraints. Although the SF-based designs used less material than the RBTO, they failed to meet the required reliability level. Furthermore, for values exceeding SF = 2, the optimizer could not achieve a feasible solution. Due to this, case-by-case comparison with RBTO results is not possible, however the example clearly illustrates the different characteristics of the methods. In the SF method, the optimizer strictly enforces stress limits without accounting for the probability of pore occurrence. In contrast, RBTO enables a more effective material layout by selectively allocating material to stochastically satisfy stress constraints. Ultimately, this demonstrates that while choosing an appropriate SF is often arbitrary and lacks a clear link to reliability, RBTO provides a rigorous framework to achieve a specific target reliability level from the start.

4.1.2 Influence of build orientation and load level

From the perspective of AM, different build orientations can be considered. For example, in this problem, applying a reverse build orientation results in a flipped temperature distribution T', where the pore occurrence probability increases from left to right (see Fig. 9a for defects representation from both temperature fields). However, in this case, it was observed that the optimizer did not obtain a feasible converged solution that meets even $\beta_t = 1$. This is attributed to the fact that, in the flipped distribution, a higher pore occurrence probability coincides with the load application area under a relatively high load level. This indicates that the spatial defect distribution is a critical factor in determining whether a feasible solution exists within this framework. Therefore, the choice of build orientation, which influences the probabilistic occurrence of pores, can have a significant effect on the reliable performance of a component.

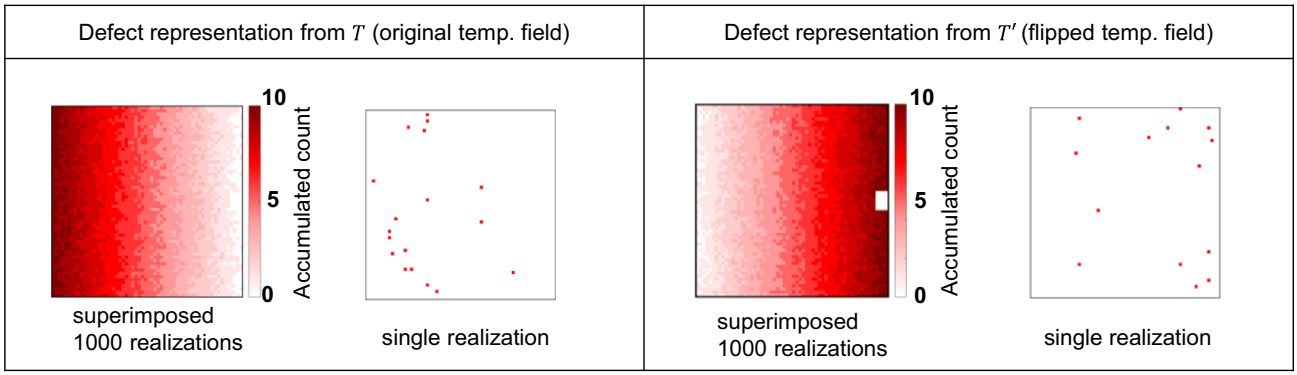
While the flipped case failed to converge under high load intensities, we further investigate the effect of different temperature fields in Fig. 9b. This figure illustrates the design evolution and trends relative to β_t across three load levels: 1.5 (low), 2.5 (intermediate), and 4 (high). The last case corresponds to the load level utilized in the examples discussed thus far. By reducing the load magnitude, feasible solutions that satisfy both the original and flipped temperature fields can be successfully obtained.

This investigation reveals two distinct trends. First, at lower load levels, the design variation across different β_t becomes less pronounced. When the load is sufficiently low, the optimizer can achieve the required reliability with minimal material addition. Second, lower loads result in a more uniform stress distribution, making the design less sensitive to the flipped temperature and pore distribution. As illustrated by the σ_{vm} field taking $\beta_t = 1$ as a representative example in Fig. 9b, high localized stress near the area of load introduction leads to the non-uniformity of the stress field as the load level increases. When the flipped temperature field is applied, designs at the low load level show almost no change, while those at the intermediate load level exhibit only minor variations. In contrast, at the high load level, no converged solution was achieved even for $\beta_t = 1$ with the flipped temperature. These results emphasize that the uniformity of the stress field significantly influences the performance and convergence of RBTO. It suggests that the choice of build orientation strategy regarding the impact of defects becomes less critical when the design maintains a uniform stress field.

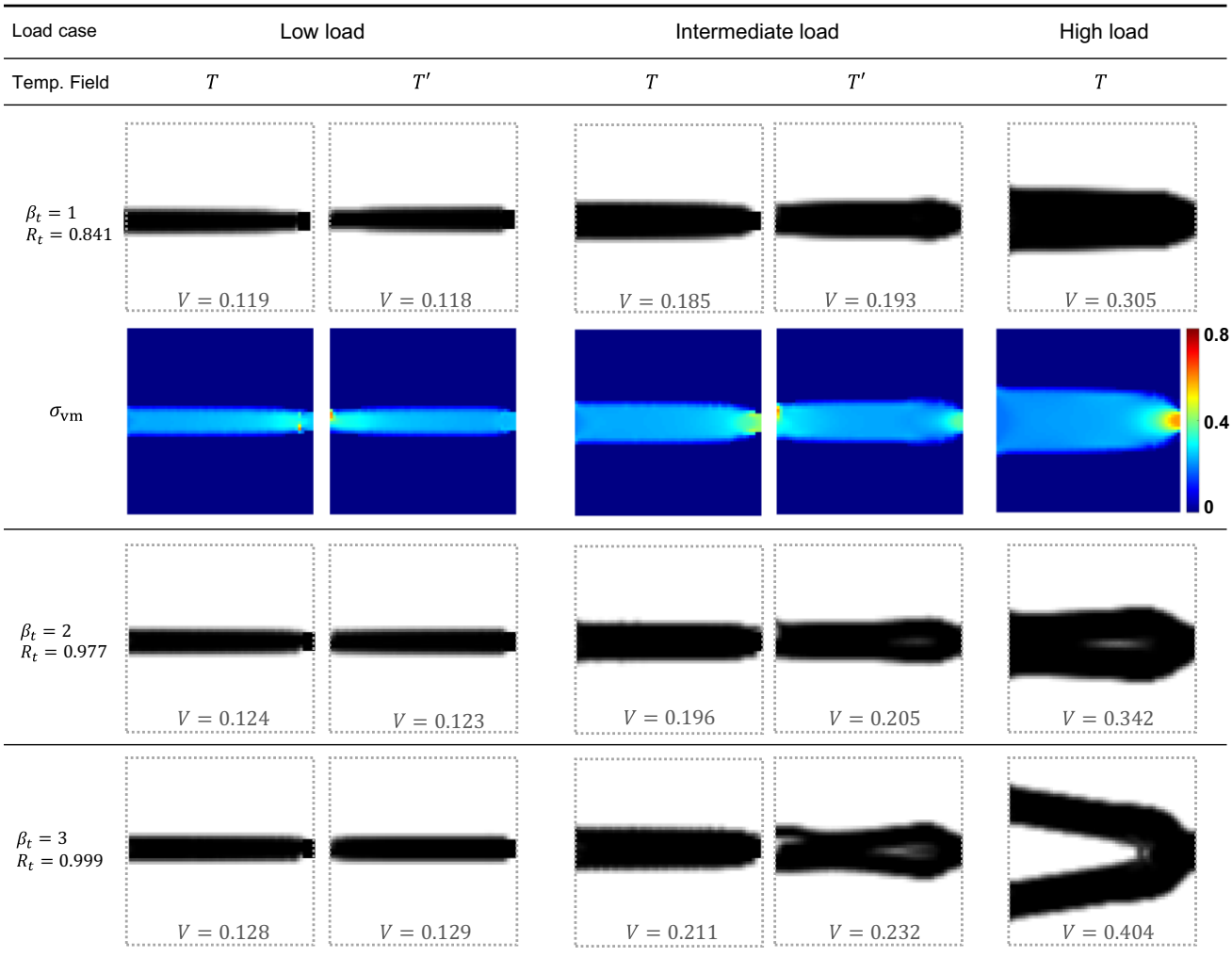
It is worth noting that at lower and intermediate loads, localized high stress occurs where the defect probability is low (specifically, σ_{vm} for temperature field T and T' in the low load and T' in the intermediate load case, as shown in Fig. 9b). The optimizer allows for high stress in areas where pores are rarely present, as this is advantageous for distributing material effectively while meeting the target failure probability, given the limited number of defect scenarios. While increasing the number of realizations could mitigate this effect in this example, we maintain the current setup to demonstrate the dependency of the proposed probabilistic method on specific defect distributions.

4.2 Example 2: half MBB

A half MBB beam problem is considered as the second example, as shown in Fig. 10a. The design domain represents the right half of the full beam and is discretized into a 120×40 mesh consisting of 4800 elements. Symmetric boundary conditions are applied at the left edge. A load of magnitude $F = 1$ is applied over 7 nodes. The allowable stress $\bar{\sigma}_{\text{a}}$ is set to 1.2. Temperature distribution is defined

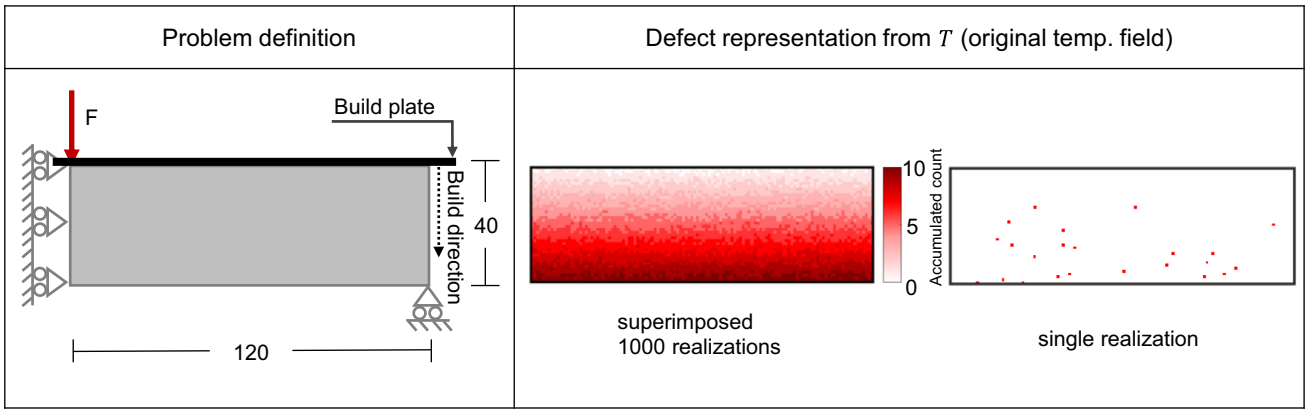


(a)



(b)

Fig. 9 Tensile bar: **a** defect representation applying T and T'; **b** optimized designs applying T and T' across three different load levels using the proposed RBTO framework, along with the corresponding von Mises stress (σ_{vm}) distribution for $\beta_t = 1$. All stress fields are scaled to $[0, 0.8]$, consistent with the allowable stress ($\bar{\sigma}_a = 0.8$)



(a)

β_t	V	Topologies	σ_{vm}	σ_{crit}
$\beta_t = 1$ $R_t = 0.841$	0.399			
$\beta_t = 2$ $R_t = 0.977$	0.410			
$\beta_t = 3$ $R_t = 0.999$	0.418			

(b)

Fig. 10 MBB beam: **a** problem definition and pore representation; **b** optimized design and stress distribution using RBTO. All the stress fields are scaled to [0, 1.2], consistent with the allowable stress ($\bar{\sigma}_{\text{a}} = 1.2$)

to increase from top to bottom across the design domain. The same probabilistic coefficients are used as in the previous tensile bar example. It must be noted that, although the design domain and boundary conditions of the MBB beam problem are symmetrical, the individual realizations of the random pore distribution are inherently asymmetrical due to their stochastic nature in reality. Nevertheless, symmetry was enforced in the optimization, and the optimized topologies were therefore constrained to remain symmetric.

In Fig. 10b, three optimized designs obtained via RBTO are presented with two stress distributions. As in the previous example, volume increases with increasing β_t. Notably, higher β_t values produce greater volume at the bottom-left of the design domain, with topology changes concentrated near this region. This example demonstrates the effect of the stress-state-dependent SCF. Unlike the tensile bar, which experiences predominantly tensile stresses, the MBB beam features complex stress states. Tensile stresses concentrate

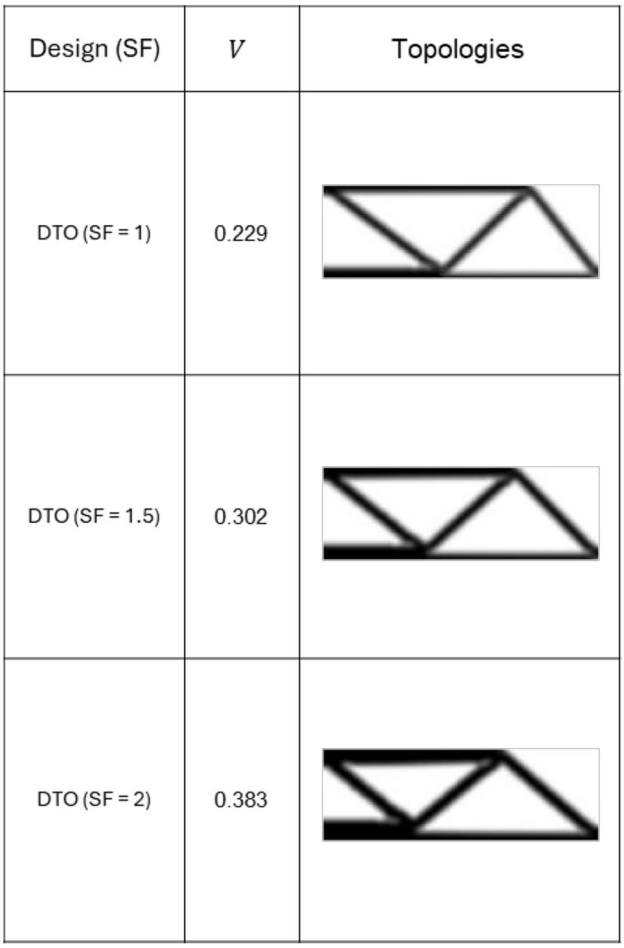


Fig. 11 MBB beam: optimized design using DTO with different safety factors (SF = 1, 1.5 and 2)

Table 4 MBB beam: reliability verification via 10^5 realizations for RBTO and SF-based designs

Method	Target	β	P_f	δ_β (%)
RBTO	$\beta_t = 1$	1.006	0.1573	+0.6
	$\beta_t = 2$	1.969	0.0245	−1.6
	$\beta_t = 3$	2.862	0.0021	−4.6
Safety factor	SF = 1	$-\infty$[a]	1.0000	–
	SF = 1.5	−2.374	0.9912	–
	SF = 2	−0.560	0.7123	–

A negative reliability index (β) indicates that the probability of failure exceeds 0.5, meaning that failure occurs in more than half of the realizations

[a]All tested samples failed for this design case

primarily in the lower-left region of the half MBB. Since the SCF weighs tensile stresses more heavily (as discussed in Sect. 2.2), the RBTO method concentrates topological changes in regions dominated by tensile stress, unlike the uniform material distribution observed in the tensile bar case. In contrast, the DTO results in Fig. 11 show uniform thickening across the structure, lacking the stress-state-dependent redistribution present in the RBTO method.

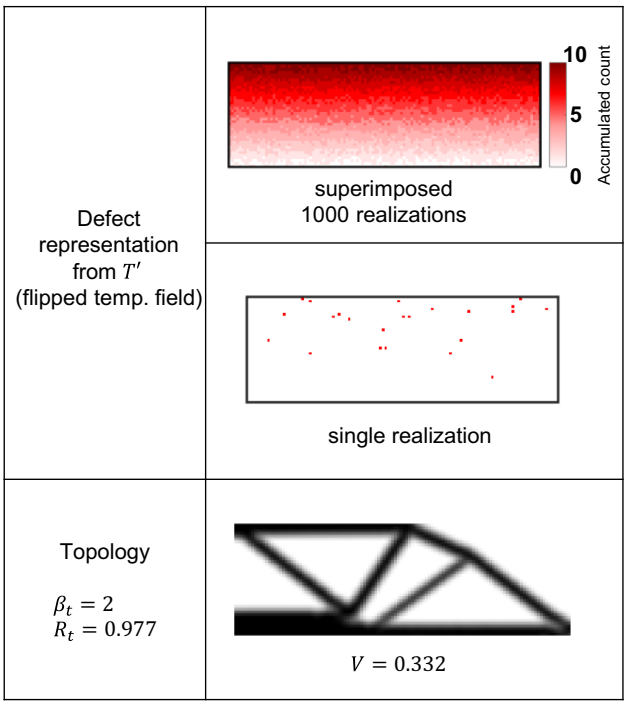


Fig. 12 MBB beam: RBTO design with flipped temperature field for $\beta_t = 2$. The optimal design achieves a reduced volume compared to the result under the original temperature field

Similar to the previous numerical example, SF-based designs achieve a reduction in volume but fail to satisfy the target reliability under defect uncertainty as discussed in Table 4. Furthermore, the optimizer again fails to reach a feasible solution for SF > 2. This underscores that simply increasing the safety factor provides no direct control over the failure probability. Moreover, it highlights the limitations of deterministic stress constraints, which fail to account for the stochastic nature of pores. For the RBTO designs, the verified reliability indices approach the target values with relative deviations ranging from $+0.6\%$ to -4.6%.

Applying a flipped build orientation reverses the temperature gradient and pore distribution probability. Under this flipped distribution, an optimal design with $\beta_t = 2$ is presented in Fig. 12 as a representative example. The RBTO design with $\beta_t = 2$ under the reversed temperature field uses 23% less material compared to the original case (the $\beta_t = 2$ design in Fig. 10b), with similar trends observed across other reliability levels. This results from the stress-state-dependent SCF, which weights pores coinciding with tensile stress more heavily. In the first build orientation, thicker members are observed in the lower region where pore occurrence probability is higher. In contrast, for the reversed build orientation, despite the higher probability of pore occurrence shifting to the upper region, similar thickening is not observed. This

Table 5 MBB beam: reliability verification of RBTO designs with reversed temperature distribution across different optimization sample sizes

	$N = 10^3$		$N = 3 \times 10^3$		$N = 10^4$	
β_t	β	δ_β (%)	β	δ_β (%)	β	δ_β (%)
1.0	0.899	−10.1	0.974	−2.6	0.982	−1.8
2.0	1.241	−37.9	1.722	−13.9	1.964	−1.8
3.0	1.628	−45.7	2.582	−13.9	3.030	+1.0

N denotes the number of realizations used during optimization. All β values are verified using a set of 10^5 realizations

is because the SCF method accounts for stress magnitude affected by pores under tensile loading as mentioned in Eq. (11).

Moreover, the flipped temperature case requires more realizations during optimization, as shown in Table 5. Since the reliability index depends on the estimated statistical moments, a larger number of samples may be required for accurate reliability estimation. This indicates that the required number of samples depends on pore distribution and underlying stress field. Specifically, when peak stress regions misalign with high-pore-probability zones (as in the flipped temperature case), the optimizer may lack sufficient information. The effects of sample size on meeting reliability levels are evaluated through MCS verification. As the number of realizations during optimization increases, the relative deviation consistently narrows across all target levels. For the case of $\beta_t = 3.0$, increasing the sample size from $N = 10^3$ to 3×10^3 and 10^4 changes the relative deviation from -45.7% to -13.9%, and ultimately to $+1.0\%$, thereby satisfying the target constraint. This indicates that within the proposed optimization framework using fixed-sampled MCS, the achievable accuracy in MCS verification is inherently sample-dependent. Furthermore, when a shortfall occurs due to sampling error in more complex problems, employing a larger sample size effectively mitigates the error and approaches the target reliability.

As shown in Fig. 13, the convergence plots for (a) DTO case and (b) RBTO case with $\beta_t = 1, 2$ and 3 are presented as representative examples. Both the objective function and the constraint show good convergence behavior for DTO and RBTO. The RBTO approach requires more iterations than DTO due to the high nonlinearity in estimating the probabilistic constraint. DTO requires 996 iterations, while RBTO with $\beta_t = 1, 2, 3$ requires 3662, 3849, and 4077 iterations, respectively.

A similar trend was observed across the other numerical examples. For the tensile bar, DTO converged in 384 iterations, whereas the most computationally intensive RBTO case ($\beta_t = 3$) required 1,636 iterations. Similarly, for the L-bracket, DTO completed in 1,171 iterations, while RBTO

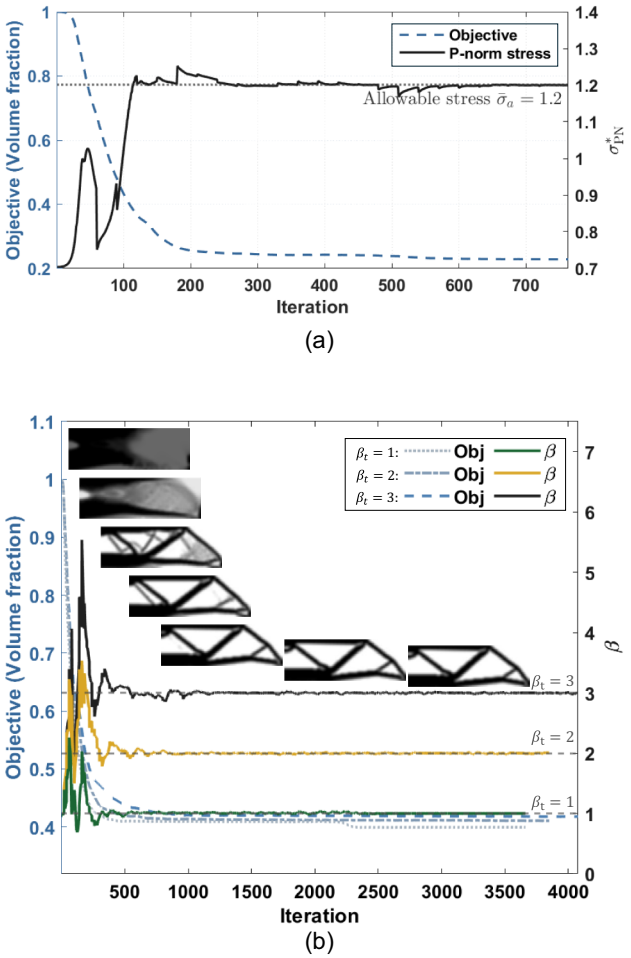
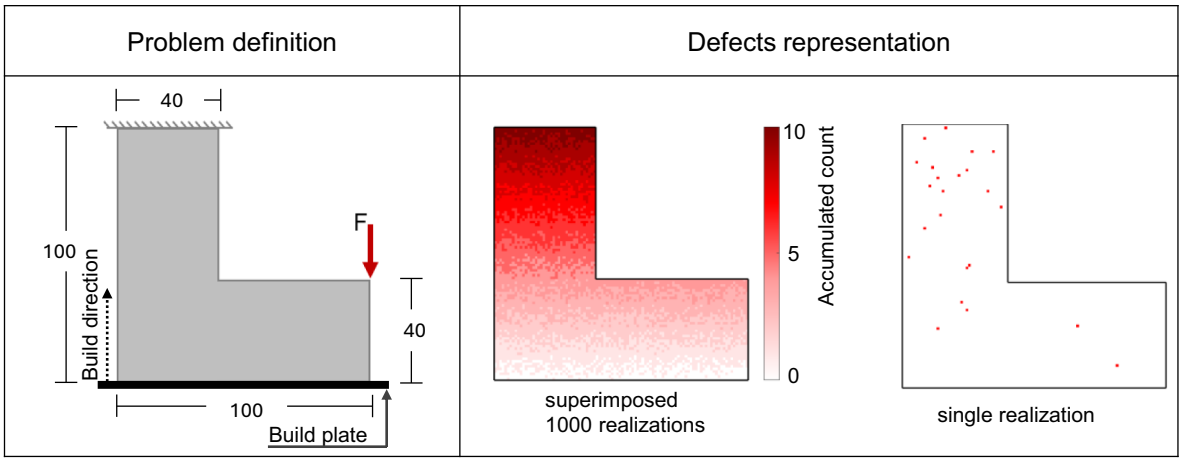
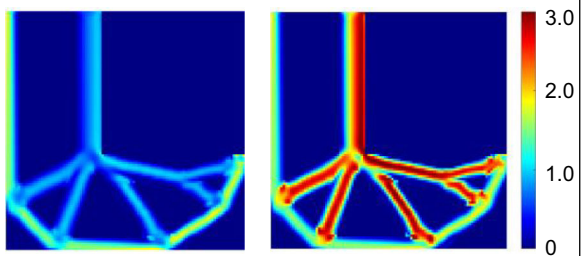
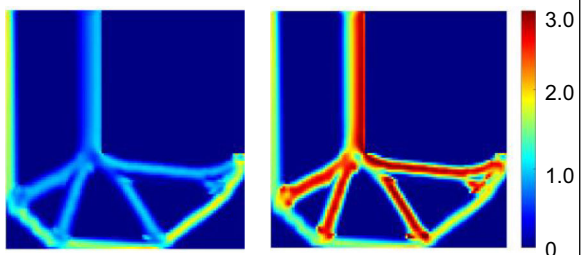
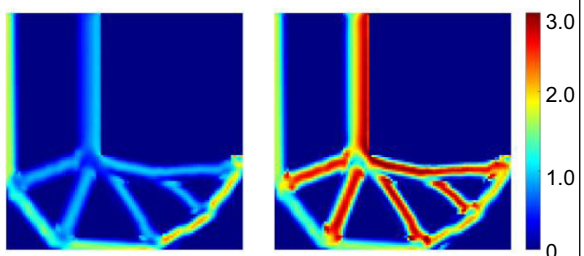


Fig. 13 Iteration history of the objective and constraint for **a** DTO design and **b** RBTO design ($\beta_t = 1, 2, 3$) for the MBB beam, showing the topology evolution at iterations 50, 100, 250, 500, 1000, 2000, and 3000 (from left to right)

with $\beta_t = 3$ required 4870 iterations. In both the DTO and RBTO cases of the MBB beam example in Fig. 13, especially in the constraint plot, regular spikes during optimization can be observed. These come from the scaling factor c, which is applied every 20 iterations, as mentioned earlier in Eq. (17). While local stress constraints inherently introduce severe nonlinearity, imposing a probabilistic constraint further increases this nonlinearity. To ensure stable convergence and prevent premature termination caused by numerical oscillations, both a small move limit and a strict convergence criterion were employed, as explained at the beginning of Sect. 4. Consequently, these rigorous settings led to a significantly longer iteration history compared to the DTO case. Fortunately, the proposed formulation, utilizing an augmented stress field obtained from a single FEA solve combined with an analytical, stress-state-dependent SCF, enables a highly cost-effective MCS implementation. This efficiency allowed the RBTO cases to converge within



(a)

β_t	V	Topologies	σ_{vm}	σ_{crit}
$\beta_t = 1$ $R_t = 0.841$	0.307			
$\beta_t = 2$ $R_t = 0.977$	0.314			
$\beta_t = 3$ $R_t = 0.999$	0.322			

(b)

Fig. 14 L-bracket: **a** problem definition and pore representation; **b** optimized design and stress distribution using RBTO. All the stress fields are scaled to [0, 3.0], consistent with the allowable stress ($\bar{\sigma}_{\text{a}} = 3.0$)

2.5 h (15 min for DTO) on an Intel Core i7-1365U CPU (1.80 GHz) and 16.0 GB of RAM. To quantify the relative computational cost of each component in the proposed framework, we profiled a representative iteration for the MBB example. The FE analysis requires 0.024 s (0.9%) per iteration, as only a single FEA is required regardless of the number of realizations. The MCS-based evaluation of the limit-state function and reliability index requires 0.416 s (16.0%), while the adjoint sensitivity assembly accounts for the remaining 2.116 s (81.4%) of the total iteration time. The MMA design variable update accounts for the remaining 0.042 s (1.6%). Although the adjoint equation itself is solved only once per iteration using a weighted factor (see Eq. (A8)), the element-wise derivative terms must still be evaluated for each of the N realizations prior to being aggregated through the statistical weights. This is the primary contributor to the computational cost.

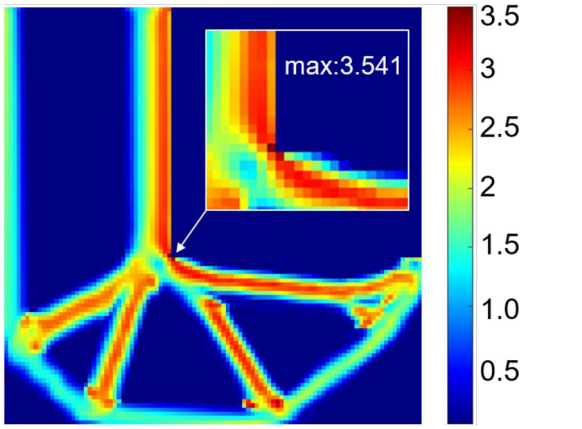


Fig. 15 L-bracket: Critical stress field σ_{crit} for the L-bracket under $\beta_t = 2.0$ (Fig. 14b). The allowable stress limit is set to 3.0, but the probabilistic stress constraint permits localized critical stresses to exceed this threshold near the re-entrant corner

4.3 Example 3: L-bracket

The L-bracket is the final example considered, with pore distribution as shown in Fig. 14a. The design domain is discretized into a total of 6400 elements. A load of magnitude $F = 2$ is applied over 5 nodes at the top right corner as shown. The allowable stress $\bar{\sigma}_{\text{a}}$ is set to 3.0.

The L-bracket is a classical benchmark for stress-based topology optimization. Under stress constraints, topologies develop rounded re-entrant corners at sharp corners to mitigate stress concentration. In Fig. 14b, all three designs exhibit less pronounced rounding near the re-entrant corner compared with the deterministic case. This is attributed to the proposed probabilistic stress constraint, which accounts for the spatial probability distribution of pores and does not require the allowable stress limit to be satisfied at every location for all possible defect scenarios. Consequently, localized stress concentrations can be accepted in regions with low defect probability while satisfying the prescribed reliability requirement. As illustrated in Fig. 15, the distribution of critical stress on a normalized scale shows that although the allowable stress limit is set to 3.0, localized critical stresses near the re-entrant corner are permitted to exceed this threshold due to the exceptionally low probability of pore formation in that region. This provides a clear insight into the difference between designs obtained under deterministic and probabilistic stress constraints. This distinguishes our approach from the traditional safety factor approach that enforces uniform, overly conservative factors without considering local defect distributions.

A notable design change with a higher β_t is the primary vertical strut in the upper half becoming slightly thicker. Two factors cause this reinforcement. First, peak stresses across realizations are most likely to occur near the re-entrant corner, requiring reinforcement in the upper strut. Second, the upper strut carries the highest tensile load within the structure, making it the most critical region. The MCS verification results in Table 6 are generally close to the target reliability. In the worst case, the deviation from the target was approximately -5% under 10^5 realizations. It should be noted that a small relative deviation in the reliability index can correspond to a larger relative deviation in the failure probability, particularly at low failure probabilities. For the L-bracket and MBB problems, some verified reliability indices deviate from the target, whereas the tensile bar problem fully satisfies the target. As demonstrated in Table 5, the sample size during optimization governs the accuracy of the reliability estimation. The sample size required for accurate reliability estimation is therefore problem-dependent. This behavior is governed by the spatial interaction between the pore distribution and stress field, which affects the accurate estimation of the statistical moments of the limit-state function. As demonstrated in Sect. 4.2, the verification gap reflects the problem-dependent nature of fixed-sample probabilistic optimization, which diminishes with larger sample sizes during optimization.

In this numerical example, we investigate the influence of the defect density, $\bar{\rho}_d$. For consistency, $\bar{\rho}_d$ is defined as the ratio of defective elements to the total number of elements in the full L-bracket domain (6400 elements), averaged over all realizations. Figure 16 shows three cases: (a) low defect density, (b) the baseline case used in the original L-bracket problem (Fig. 14), and (c) high defect density. Different defect densities are obtained by adjusting $p_{i,\min}$ and $p_{i,\max}$ as summarized in Table 7. As expected, defect density affects the optimized volume, as shown in Table 8. Low defect density enables material savings. However, within each defect density level, the effect of the RBTO framework differs significantly. Only in high defect density cases,

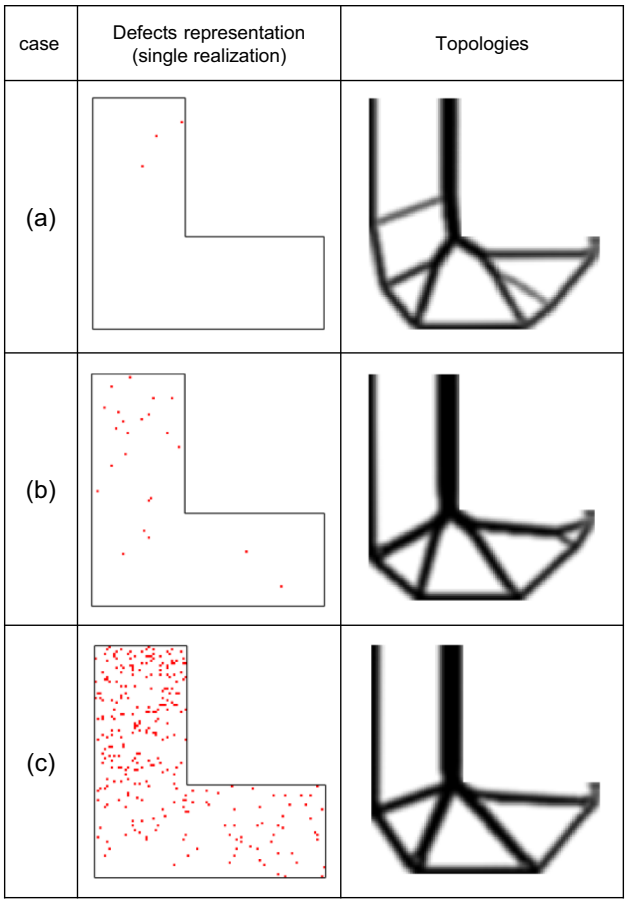


Fig. 16 L-bracket: RBTO designs at $\beta_t = 2$ for three defect densities: **a** 0.0458%, **b** 0.398% (baseline), **c** 4.485%

nearly identical topologies and volume are achieved across different reliability indices. This behavior can be explained by the low standard deviation of σ^*_{PN} values in Table 8. This occurs because high defect density consistently captures peak stresses at the area near the corner, regardless of pore distribution variations. Additionally, with very low defect density in case (a), more realizations are needed to satisfy the target reliability than in cases (b) and (c).

Moving from Sects. 4.1 to 4.3, the effect on the resulting volume reduces. This is related to the inherent high-stress regions involved in the problem. Specifically, in the L-bracket case, the stress near the re-entrant corner is already critical, but due to the tensile SCF effect after pore generation, it becomes much more significant. If a prominent high-stress area is present in the design, it dominates the optimization, as any defect in those high-stress regions will define the maximum stress.

Depending on the chosen AM technology, most of the optimized designs presented herein might require support structures, considering the designated build plate locations and resulting overhang features. In such cases, for practical AM considerations, fabrication restrictions, such as restricting overhangs or employing a self-supporting structure, can be readily incorporated (Langelaar 2016; Gaynor and Guest 2016; Langelaar 2017). Because the present study focuses on reliability under stochastic porosity uncertainty, explicit manufacturability constraints are left for future work.

Table 6 L-bracket: reliability verification via 10^5 realizations for RBTO designs

β_t	β	P_f	δ_β (%)
1	0.9885	0.1615	−1.2
2	1.9552	0.0253	−2.2
3	2.8501	0.0022	−5.0

Table 7 L-bracket: parameters for the temperature-dependent probabilistic pore model across varying defect densities

Case	$p_{i,\min}$	$p_{i,\max}$
(a) Lower defect density	10^{-5}	10^{-3}
(b) Baseline	10^{-4}	10^{-2}
(c) Higher defect density	10^{-2}	10^{-1}

Table 8 L-bracket: RBTO results at $\beta_t = 2$ with different defect densities

Case	Defect density ($\bar{\rho}_d$)	V	N	St-Dev(σ^*_{PN})
(a)	0.0458%	0.260	3×10^3	0.246
(b)	0.398%	0.314	10^3	0.131
(c)	4.485%	0.329	10^3	0.061

N denotes the number of realizations used during optimization

As a final investigation, rather than completely flipping the temperature field by placing the build plate on the opposite side, we extended our study to include the 45° and 135° build directions shown in Fig. 17. For this analysis, the baseline design utilizes the L-bracket with $\beta_t = 3$ (in Fig. 14b), which originally employed a 90° build direction with the build plate at the bottom. It is worth noting that rotating the build direction alters the maximum distance from the build plate, thereby affecting the corresponding defect distribution. Regarding optimized design and volume fraction, only minor variations are observed. The volume is 0.329 for the 45° build direction case, 0.328 for the 135° build direction case, and 0.322 for the 90° build direction case (the baseline). This behavior is expected for the L-bracket problem. As previously mentioned, owing to the geometric nature of the re-entrant corner, peak stresses across random pore realizations are statistically most likely to occur near this corner and the adjacent strut. Since this critical region remains near the mid-height of the design domain for all considered build directions, the defect probability within this dominant stress-concentration region changes only moderately. In terms of the reliability index, a deviation from the target is observed. For the 45° and 135° cases, the reliability indices verified using

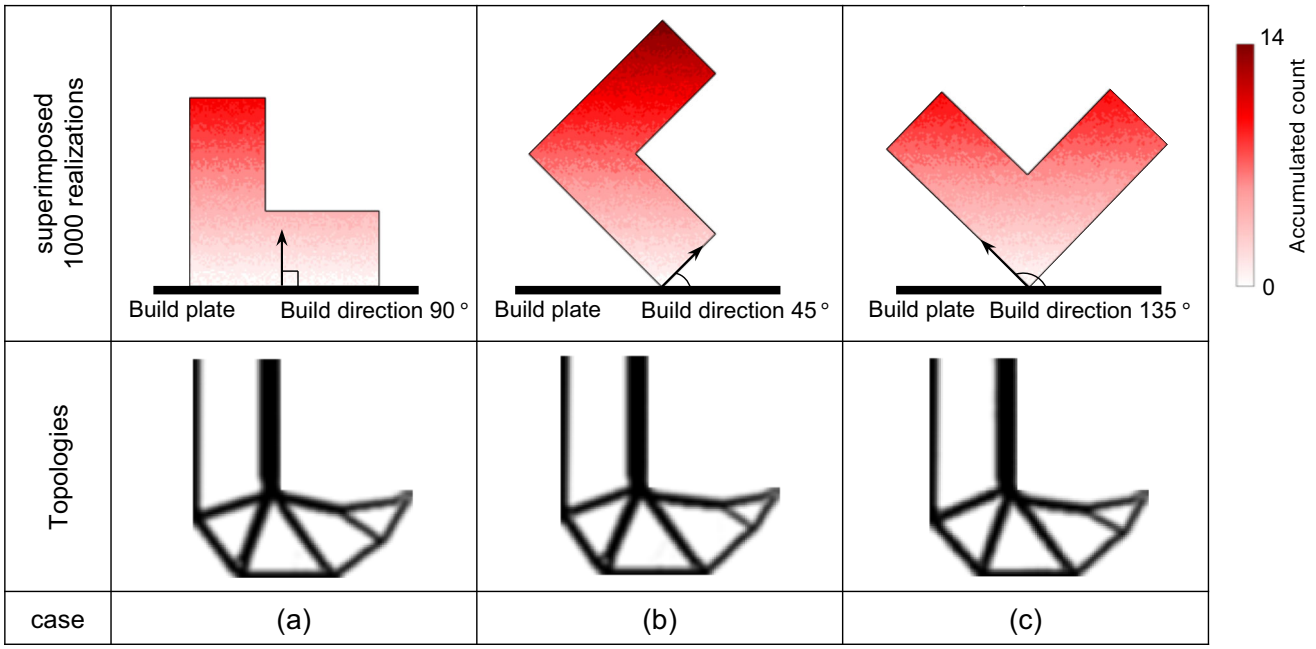


Fig. 17 L-bracket: optimization results under various build directions: **a** build direction 90°, **b** build direction 45°, and **c** build direction 135°. The upper row presents the overall spatial tendency of the defect distribution, represented by the superposition of 10^3 defect realizations generated according to each build direction. The lower row shows the corresponding optimized topologies for $\beta_t = 3$

10^5 realizations are 2.812 and 2.931, respectively. Consistent with the discussion in Sect. 4.2, this verification gap stems from problem-dependent sampling effects.

5 Conclusion and future work

This study presents an RBTO framework to address stochastic porosity defects occurring in AM in a computationally efficient manner. While pore-induced stress concentration significantly compromises the structural integrity, this process-related uncertainty has not been directly addressed in topology optimization. We addressed this uncertainty by modeling stochastic porosity. By combining a temperature-dependent stochastic pore model with analytical stress-state-dependent SCFs, the proposed method evaluates a large number of Monte Carlo pore realizations by analytically augmenting the pore-free stress field, requiring only a single FE analysis per optimization iteration rather than a separate FE analysis for each realization.

Numerical results demonstrate the effectiveness of the proposed RBTO framework in satisfying the target reliability index under uncertain pores. For comparison, safety factor (SF)-based designs are presented. While SF-based designs may achieve volume reductions, they can fail to satisfy the target reliability under defect uncertainty. This work clearly shows the limitations of the deterministic design method, which fails to account for the stochastic nature of pores. Furthermore, the SF-based approach fails to reach a feasible solution at higher SF. This underscores that simply increasing SF is not a fundamental solution for ensuring structural reliability. Moreover, choosing an appropriate SF is often arbitrary and lacks a direct link to the target reliability. Conversely, RBTO provides a systematic framework to achieve a specific target reliability level from the start.

Additionally, the presented RBTO examples demonstrate that the spatial pore distribution in AM, which results from different build orientations, significantly influences RBTO performance by affecting both the required sample size and the resulting volume. Notably, the stress-state-dependent SCF plays a critical role; because pore-induced stress magnitudes are more pronounced under tensile loading, the optimizer can strategically distribute material to satisfy the target failure probability. These findings suggest that careful consideration must be given to the build-orientation strategy for AM fabrication when accounting for defect uncertainty.

Another interesting observation is that inherently prominent high-stress regions, such as the re-entrant corners in the L-bracket case, tend to dominate the optimization process when a higher number of defects is expected. Since any defect within these critical areas dictates the maximum stress, no significant volume change is required with increasing target reliability index. Moreover, the influence of the defect distribution induced by the temperature field depends on the stress distribution in the optimized design. When the stress

field is relatively uniform, altering the temperature distribution has little effect on the resulting volume.

A sample size of 10^3 realizations may be insufficient to accurately estimate the statistical moments of the limit-state function, potentially leading to solutions that do not satisfy the target reliability requirements. Although increasing the sample size during optimization is shown to diminish this verification gap, as demonstrated in Sect. 4.2, the ideal sample size required to prevent such issues cannot be easily determined a priori. To address this challenge, exploring alternative uncertainty quantification methods is a promising direction for future research.

Another important extension for future research is related to the current assumptions in stochastic pore modeling. For simplicity, the probability of pore formation was based on a pre-defined linear temperature field increasing with the distance from the build plate, without fully accounting for spatial correlations in pore distribution and realistic AM conditions. Therefore, future studies will aim to incorporate a design-dependent temperature field to accurately account for realistic AM-induced defects. Additionally, extending from 2D to 3D is an essential step in developing RBTO for practical AM applications.

Appendix A Sensitivity analysis

This section is divided into three subsections to reduce the complexity of the sensitivity analysis. In the first subsection, the derivative of the statistical moment-based constraint with respect to the design variable is discussed. The second subsection presents a practical strategy for efficient adjoint sensitivity computation using statistical weights. Finally, in the third subsection, the sensitivity of the P-norm stress with respect to the design variable is derived by using the adjoint method.

A.1 Derivative of constraint via statistical moments

The mean and variance are computed using MCS as follows:

$$\mu_G = \frac{1}{N}\sum_{j=1}^{N} G(\boldsymbol{\rho}, \mathbf{X}^{(j)}) \tag{A1}$$

$$\sigma_G^2 = \frac{1}{N-1}\sum_{j=1}^{N}\left(G(\boldsymbol{\rho}, \mathbf{X}^{(j)}) - \mu_G\right)^2 \tag{A2}$$

The reliability index β is defined as the ratio of the mean to the standard deviation of the limit state function as follows:

$$\beta = \frac{\mu_G}{\sigma_G} \tag{A3}$$

Accordingly, the derivative of the constraint with respect to the design variable ρ_e is calculated as follows:

$$\frac{\partial \beta}{\partial \rho_e} = \frac{1}{\sigma_G}\frac{\partial \mu_G}{\partial \rho_e} - \frac{\mu_G}{\sigma_G^2}\left(\frac{1}{2\sigma_G}\frac{\partial \sigma_G^2}{\partial \rho_e}\right) \tag{A4}$$

Here, the derivative of the variance is used instead of the standard deviation for ease of calculation.

As shown in Eq. (A4), the derivatives of the statistical moments are required, and they are given below.

$$\frac{\partial \mu_G}{\partial \rho_e} = \frac{1}{N}\sum_{j=1}^{N}\frac{\partial G(\boldsymbol{\rho}, \mathbf{X}^{(j)})}{\partial \rho_e} \tag{A5}$$

$$\frac{\partial \sigma_G^2}{\partial \rho_e} = \frac{2}{N-1}\sum_{j=1}^{N}\left(G(\boldsymbol{\rho}, \mathbf{X}^{(j)}) - \mu_G\right)\left(\frac{\partial G(\boldsymbol{\rho}, \mathbf{X}^{(j)})}{\partial \rho_e} - \frac{\partial \mu_G}{\partial \rho_e}\right) \tag{A6}$$

By substituting Eqs. (A5) and (A6) into Eq. (A4), the derivative of the constraint can be expressed as follows:

$$\frac{\partial \beta}{\partial \rho_e} = \frac{1}{\sigma_G}\frac{1}{N}\sum_{j=1}^{N}\frac{\partial G(\boldsymbol{\rho}, \mathbf{X}^{(j)})}{\partial \rho_e} - \mu_G\frac{1}{2\sigma_G^3}\frac{1}{N-1}\sum_{j=1}^{N}2(G(\boldsymbol{\rho}, \mathbf{X}^{(j)}) - \mu_G)\left(\frac{\partial G(\boldsymbol{\rho}, \mathbf{X}^{(j)})}{\partial \rho_e} - \frac{\partial \mu_G}{\partial \rho_e}\right) \tag{A7}$$

A.2 Practical strategy for efficient adjoint sensitivity computation

Even in the proposed RBTO framework, where an efficient SCF estimation requires only one FEA to achieve N stress mappings for N realizations, the same efficiency does not hold for the adjoint sensitivity analysis. The adjoint loads can first be summed using the statistical coefficients. The adjoint equation is then solved only once, resulting in a single adjoint sensitivity analysis. To achieve this, the statistical coefficient (w_j) is derived as follows.

$$\frac{\partial \beta}{\partial \rho_e} = \sum_{j=1}^{N}\left(\frac{\partial G(\boldsymbol{\rho}, \mathbf{X}^{(j)})}{\partial \rho_e}\right) \times \underbrace{\left[\frac{1}{N\sigma_G} - \frac{\mu_G}{(N-1)\sigma_G^3}\left(G(\boldsymbol{\rho}, \mathbf{X}^{(j)}) - \mu_G\right)\right]}_{w_j} \tag{A8}$$

A.3 Sensitivity analysis for stress-related term

Since in Sect. A.1, the derivative of the constraint is expressed in terms of statistical moments and the derivative of the limit state function, this section focuses on the detailed sensitivity analysis.

First, by the definition of the limit state function in Eq. (22), the derivative of $G(\boldsymbol{\rho}, \mathbf{X})$ is expressed in terms of the pore-induced P-norm stress as follows:

$$\frac{\partial G(\boldsymbol{\rho}, \mathbf{X})}{\partial \rho_e} = -c \, \frac{\partial \sigma^*_{\mathrm{PN}}(\boldsymbol{\rho}, \mathbf{X})}{\partial \rho_e} \tag{A9}$$

The derivative of the pore-induced P-norm stress with respect to the design variable can be expressed using the chain rule:

$$\frac{\partial \sigma^*_{\mathrm{PN}}(\boldsymbol{\rho}, \mathbf{X})}{\partial \rho_e} = \sum_{i=1}^{n} \frac{\partial \sigma^*_{\mathrm{PN}}(\boldsymbol{\rho}, \mathbf{X})}{\partial \sigma^*_{\mathrm{vm},i}} \frac{\partial \sigma^*_{\mathrm{vm},i}}{\partial \rho_e} \tag{A10}$$

Depending on the indicator variable I_i defined in Eq. (2), the term $\frac{\partial \sigma^*_{\mathrm{vm},i}}{\partial \rho_e}$ is expressed differently, as shown below,

$$\begin{aligned} \frac{\partial \sigma^*_{\mathrm{vm},i}}{\partial \rho_e} &= \frac{\partial \sigma^*_{\mathrm{vm},i}}{\partial \hat{\boldsymbol{\sigma}}_i} \left(\frac{\partial \eta_s(\rho_i)}{\partial \rho_e} \boldsymbol{\sigma}_i + \eta_s(\rho_i) \frac{\partial \boldsymbol{\sigma}_i}{\partial \rho_e} \right) \\ &= \frac{\partial \sigma^*_{\mathrm{vm},i}}{\partial \hat{\boldsymbol{\sigma}}_i} \frac{\partial \eta_s(\rho_i)}{\partial \rho_e} \boldsymbol{\sigma}_i + \frac{\partial \sigma^*_{\mathrm{vm},i}}{\partial \hat{\boldsymbol{\sigma}}_i} \eta_s(\rho_i) \frac{\partial \boldsymbol{\sigma}_i}{\partial \rho_e} \end{aligned} \tag{A11}$$

with,

$$\frac{\partial \sigma^*_{\mathrm{vm},i}}{\partial \hat{\boldsymbol{\sigma}}_i} = \begin{cases} \frac{\partial \sigma_{\mathrm{vm},i}}{\partial \hat{\boldsymbol{\sigma}}_i}, & i \in \Omega_0 \\ \frac{\partial \sigma_{\mathrm{crit},i}}{\partial \hat{\boldsymbol{\sigma}}_i}, & i \in \Omega_1 \end{cases} \tag{A12}$$

The chain rule for the relaxed stress vector in Eq. (A11) is applied in the same manner, except for the term $\frac{\partial \sigma^*_{\mathrm{vm},i}}{\partial \hat{\boldsymbol{\sigma}}_i}$, which depends on whether the element i belongs to the pore-free region Ω_0 or the pore-affected region Ω_1. For elements in Ω_0, the standard von Mises stress derivative is used, while for elements in Ω_1, the derivative of the critical stress is applied. As the case Ω_1 follows a similar procedure, only the case Ω_0 is presented here. The derivation of $\frac{\partial \sigma_{\mathrm{crit},i}}{\partial \hat{\boldsymbol{\sigma}}_i}$ is provided later in this section.

For elements in Ω_0, by substituting Eq. (A12) into Eq. (A11), and subsequently into Eq. (A10), the following expression is obtained:

$$\begin{aligned} \frac{\partial \sigma^*_{\mathrm{PN}}(\boldsymbol{\rho}, X)}{\partial \rho_e} &= \sum_{i=1}^{n} \frac{\partial \sigma^*_{\mathrm{PN}}}{\partial \sigma^*_{\mathrm{vm},i}} \frac{\partial \sigma^*_{\mathrm{vm},i}}{\partial \rho_e} \\ &= \sum_{i=1}^{n} \frac{\partial \sigma^*_{\mathrm{PN}}}{\partial \sigma^*_{\mathrm{vm},i}} \left(\frac{\partial \sigma^*_{\mathrm{vm},i}}{\partial \hat{\boldsymbol{\sigma}}_i} \frac{\partial \eta_s(\rho_i)}{\partial \rho_e} \boldsymbol{\sigma}_i \right. \\ &\quad \left. + \frac{\partial \sigma^*_{\mathrm{vm},i}}{\partial \hat{\boldsymbol{\sigma}}_i} \eta_s(\rho_i) \frac{\partial \boldsymbol{\sigma}_i}{\partial \rho_e} \right) \end{aligned} \tag{A13}$$

Since we defined the P-norm stress in Eq. (20), the $\frac{\partial \sigma^*_{\mathrm{PN}}}{\partial \sigma^*_{\mathrm{vm},i}}$ is expressed as follows:

$$\frac{\partial \sigma^*_{\mathrm{PN}}}{\partial \sigma^*_{\mathrm{vm},i}} = \left(\sum_{i=1}^{n} (\sigma^*_{\mathrm{vm},i})^P \right)^{\frac{1}{P}-1} (\sigma^*_{\mathrm{vm},i})^{P-1}. \tag{A14}$$

Based on the definition of von Mises stress in Eq. (16), the derivative of von Mises stress with respect to stress component becomes,

$$\begin{aligned} \frac{\partial \hat{\sigma}_{\mathrm{vm},i}}{\partial \hat{\sigma}_{ix}} &= \frac{1}{2\hat{\sigma}_{\mathrm{vm},i}} \left(2\hat{\sigma}_{ix} - \hat{\sigma}_{iy} \right) \\ \frac{\partial \hat{\sigma}_{\mathrm{vm},i}}{\partial \hat{\sigma}_{iy}} &= \frac{1}{2\hat{\sigma}_{\mathrm{vm},i}} \left(2\hat{\sigma}_{iy} - \hat{\sigma}_{ix} \right) \\ \frac{\partial \hat{\sigma}_{\mathrm{vm},i}}{\partial \hat{\tau}_{ixy}} &= \frac{3}{\hat{\sigma}_{\mathrm{vm},i}} \hat{\tau}_{ixy} \end{aligned} \tag{A15}$$

Based on Eq. (13), the derivative of $\eta_s(\rho_i)$ with respect to the design variable in Eq. (A13) is given by:

$$\frac{\partial \eta_s(\rho_i)}{\partial \rho_e} = q(\rho_e)^{q-1} \delta_{ie} \tag{A16}$$

where δ_{ie} is the Kronecker delta ($\delta_{ie} = 1$ if $i = e$, and 0 otherwise).

The stress vector is defined by the constitutive matrix $\mathbf{D}$ based on the non-penalized Young's modulus, the strain–displacement matrix $\mathbf{B}_i$ and the local displacement $\mathbf{u}_i$ at each element as follows:

$$\boldsymbol{\sigma}_i = \mathbf{D}\mathbf{B}_i \mathbf{u}_i \tag{A17}$$

Accordingly, the derivative of the stress vector is given by,

$$\frac{\partial \boldsymbol{\sigma}_i}{\partial \rho_e} = \mathbf{D}\mathbf{B}_i \frac{\partial \mathbf{u}_i}{\partial \rho_e} \tag{A18}$$

By substituting Eqs. (A15)–(A18) into Eq. (A13)

$$\begin{aligned} \frac{\partial \sigma^*_{\mathrm{PN}}}{\partial \rho_e} = \sum_{i=1}^{n} \frac{\partial \sigma^*_{\mathrm{PN}}}{\partial \sigma^*_{\mathrm{vm},i}} \left(\left(\frac{\partial \sigma_{\mathrm{vm},i}}{\partial \hat{\boldsymbol{\sigma}}_i} \right)^T \frac{\partial \eta_s(\rho_i)}{\partial \rho_e} \mathbf{D}\mathbf{B}_i \mathbf{u}_i \right. \\ \left. + \left(\frac{\partial \sigma_{\mathrm{vm},i}}{\partial \hat{\boldsymbol{\sigma}}_i} \right)^T \eta_s(\rho_i) \mathbf{D}\mathbf{B}_i \mathbf{L}_i \frac{\partial \mathbf{U}}{\partial \rho_e} \right) \end{aligned} \tag{A19}$$

To apply the adjoint method for sensitivity analysis, $\frac{\partial \mathbf{U}}{\partial \rho_e}$ is substituted by $-\mathbf{K}^{-1} \frac{\partial \mathbf{K}}{\partial \rho_e} \mathbf{U}$. Accordingly, the adjoint variable $\boldsymbol{\lambda}$ is defined as,

$$\boldsymbol{\lambda}^T = \sum_{i=1}^{n} \eta_s(\rho_i) \frac{\partial \sigma^*_{\mathrm{PN}}}{\partial \sigma^*_{\mathrm{vm},i}} \left(\frac{\partial \sigma_{\mathrm{vm},i}}{\partial \hat{\boldsymbol{\sigma}}_i} \right)^T \mathbf{D}\mathbf{B}_i \mathbf{L}_i \mathbf{K}^{-1} \tag{A20}$$

Thus, the adjoint variable can be computed as follows:

$$\mathbf{K}\boldsymbol{\lambda} = \sum_{i=1}^{n} \eta_s(\rho_i) \frac{\partial \sigma^*_{\mathrm{PN}}}{\partial \sigma^*_{\mathrm{vm},i}} (\mathbf{DB}_i \mathbf{L}_i)^T \left(\frac{\partial \sigma_{\mathrm{vm},i}}{\partial \hat{\boldsymbol{\sigma}}_i} \right) \tag{A21}$$

After obtaining the adjoint variable $\boldsymbol{\lambda}$ using Eq. (A21), then Eq. (A19) is simplified as,

$$\frac{\partial \sigma^*_{\mathrm{PN}}}{\partial \rho_e} = \sum_{i=1}^{n} \frac{\partial \sigma^*_{\mathrm{PN}}}{\partial \sigma^*_{\mathrm{vm},i}} \left(\frac{\partial \sigma_{\mathrm{vm},i}}{\partial \hat{\boldsymbol{\sigma}}_i} \right)^T \frac{\partial \eta_s(\rho_i)}{\partial \rho_e} \mathbf{DB}_i \mathbf{u}_i - \boldsymbol{\lambda}^T \frac{\partial \mathbf{K}}{\partial \rho_e} \mathbf{U} \tag{A22}$$

At the end, the derivative of the limit state function in Eq. (A9) can be obtained using Eq. (A22). With this, the derivative of the constraint in Eq. (A7) can be computed.

For elements in Ω_1, the adjoint method is applied in the same manner. The only modification is to replace the term $\frac{\partial \sigma_{\mathrm{vm},i}}{\partial \hat{\boldsymbol{\sigma}}_i}$ in Eq. (A13) with $\frac{\partial \sigma_{\mathrm{crit},i}}{\partial \hat{\boldsymbol{\sigma}}_i}$, which is derived based on the definition of $\sigma_{\mathrm{crit},i}$ given in Eq. (11):

$$\frac{\partial \sigma_{\mathrm{crit},i}}{\partial \hat{\boldsymbol{\sigma}}_i} = \frac{1}{2} \left(1 + \frac{\sigma^{\max}_{\theta\theta,i} - \hat{\sigma}_{\mathrm{vm},i}}{\sqrt{(\sigma^{\max}_{\theta\theta,i} - \hat{\sigma}_{\mathrm{vm},i})^2 + \epsilon}} \right) \frac{\partial \sigma^{\max}_{\theta\theta,i}}{\partial \hat{\boldsymbol{\sigma}}_i} + \frac{1}{2} \left(1 - \frac{\sigma^{\max}_{\theta\theta,i} - \hat{\sigma}_{\mathrm{vm},i}}{\sqrt{(\sigma^{\max}_{\theta\theta,i} - \hat{\sigma}_{\mathrm{vm},i})^2 + \epsilon}} \right) \frac{\partial \hat{\sigma}_{\mathrm{vm},i}}{\partial \hat{\boldsymbol{\sigma}}_i} \tag{A23}$$

$\frac{\partial \hat{\sigma}_{\mathrm{vm},i}}{\partial \hat{\boldsymbol{\sigma}}_i}$ is derived in Eq. (A15). The derivative of $\sigma^{\max}_{\theta\theta,i}$ with respect to stress component is given as follows:

$$\begin{aligned}
\frac{\partial \sigma^{\max}_{\theta\theta,i}}{\partial \hat{\sigma}_{ix}} &= 1 + \frac{2(\hat{\sigma}_{ix} - \hat{\sigma}_{iy})}{\sqrt{(\hat{\sigma}_{ix} - \hat{\sigma}_{iy})^2 + 4\hat{\tau}^2_{ixy}}} \\
\frac{\partial \sigma^{\max}_{\theta\theta,i}}{\partial \hat{\sigma}_{iy}} &= 1 - \frac{2(\hat{\sigma}_{ix} - \hat{\sigma}_{iy})}{\sqrt{(\hat{\sigma}_{ix} - \hat{\sigma}_{iy})^2 + 4\hat{\tau}^2_{ixy}}} \\
\frac{\partial \sigma^{\max}_{\theta\theta,i}}{\partial \hat{\tau}_{ixy}} &= \frac{8\hat{\tau}_{ixy}}{\sqrt{(\hat{\sigma}_{ix} - \hat{\sigma}_{iy})^2 + 4\hat{\tau}^2_{ixy}}}
\end{aligned} \tag{A24}$$

In this case the adjoint variable can be computed as,

$$\boldsymbol{\lambda}^T = \sum_{i=1}^{n} \eta_s(\rho_i) \frac{\partial \sigma^*_{\mathrm{PN}}}{\partial \sigma^*_{\mathrm{vm},i}} \left(\frac{\partial \sigma_{\mathrm{crit},i}}{\partial \hat{\boldsymbol{\sigma}}_i} \right)^T \mathbf{DB}_i \mathbf{L}_i \mathbf{K}^{-1} \tag{A25}$$

Compared with Eq. (A20), only the term $\frac{\partial \sigma_{\mathrm{crit},i}}{\partial \hat{\boldsymbol{\sigma}}_i}$ needs to be computed instead of $\frac{\partial \sigma_{\mathrm{vm},i}}{\partial \hat{\boldsymbol{\sigma}}_i}$.

Acknowledgements The authors would like to express their gratitude to Krister Svanberg for making the MMA MATLAB code available.

Author Contributions YP: Conceptualization, methodology, software, analysis, writing—original draft. ON: Conceptualization, methodology, writing—review and editing, supervision. ML: Conceptualization, methodology, writing—review and editing, supervision.

Funding No funding was received to assist with the preparation of this manuscript.

Declarations

Replication of results The necessary information for replication of the results is provided in this manuscript. Further algorithm details or data are available from the corresponding author upon reasonable request.

Conflict of interest The authors have no relevant financial or non-financial interests to disclose.

Open Access This article is licensed under a Creative Commons Attribution 4.0 International License, which permits use, sharing, adaptation, distribution and reproduction in any medium or format, as long as you give appropriate credit to the original author(s) and the source, provide a link to the Creative Commons licence, and indicate if changes were made. The images or other third party material in this article are included in the article's Creative Commons licence, unless indicated otherwise in a credit line to the material. If material is not included in the article's Creative Commons licence and your intended use is not permitted by statutory regulation or exceeds the permitted use, you will need to obtain permission directly from the copyright holder. To view a copy of this licence, visit http://creativecommons.org/licenses/by/4.0/.

References

Afroz L, Inverarity S, Qian M, Easton M, Das R (2024) Analysing the effect of defects on stress concentration and fatigue life of L-PBF AlSi10Mg alloy using finite element modelling. Prog Addit Manuf 9(2):341–359. https://doi.org/10.1007/s40964-023-00457-0

Al-Maharma AY, Patil SP, Markert B (2020) Effects of porosity on the mechanical properties of additively manufactured components: a critical review. Mater Res Express 7(12):122001. https://doi.org/10.1088/2053-1591/abcc5d

Bayat M, Thanki A, Mohanty S, Witvrouw A, Yang S, Thorborg J, Tiedje NS, Hattel JH (2019) Keyhole-induced porosities in laser-based powder bed fusion (L-PBF) of Ti6Al4V: high-fidelity modelling and experimental validation. Addit Manuf 30:100835. https://doi.org/10.1016/j.addma.2019.100835

Biswal R, Syed AK, Zhang X (2018) Assessment of the effect of isolated porosity defects on the fatigue performance of additive manufactured titanium alloy. Addit Manuf 23:433–442. https://doi.org/10.1016/j.addma.2018.08.024

Bruggi M, Duysinx P (2012) Topology optimization for minimum weight with compliance and stress constraints. Struct Multidisc Optim 46:369–384. https://doi.org/10.1007/s00158-012-0759-7

Bruns TE, Tortorelli DA (2001) Topology optimization of non-linear elastic structures and compliant mechanisms. Comput Methods Appl Mech Eng 190(26–27):3443–3459. https://doi.org/10.1016/S0045-7825(00)00278-4

Chen P, Lei Z, Li G, Meng Z, Yang D (2026) Robust discrete variable topology optimization for continuum structures under load and

material uncertainties. Struct Multidisc Optim 69(3):60. https://doi.org/10.1007/s00158-026-04264-3
Cook PS, Murphy AB (2020) Simulation of melt pool behaviour during additive manufacturing: Underlying physics and progress. Addit Manuf 31:100909. https://doi.org/10.1016/j.addma.2019.100909
da Silva GA, Beck AT, Sigmund O (2019) Topology optimization of compliant mechanisms with stress constraints and manufacturing error robustness. Comput Methods Appl Mech Eng 354:397–421. https://doi.org/10.1016/j.cma.2019.05.046
Davis T, Healy D, Bubeck A, Walker R (2017) Stress concentrations around voids in three dimensions: the roots of failure. J Struct Geol 102:193–207. https://doi.org/10.1016/j.jsg.2017.07.013
Diegel O, Nordin A, Motte D (2020) A practical guide to design for additive manufacturing. Springer. https://doi.org/10.1007/978-981-13-8281-9
Duysinx P, Sigmund O (1998) New developments in handling stress constraints in optimal material distribution. In: 7th AIAA/USAF/NASA/ISSMO symposium on multidisciplinary analysis and optimization, p 4906. https://doi.org/10.2514/6.1998-4906
Galarraga H, Lados DA, Dehoff RR, Kirka MM, Nandwana P (2016) Effects of the microstructure and porosity on properties of Ti-6Al-4V ELI alloy fabricated by electron beam melting (EBM). Addit Manuf 10:47–57. https://doi.org/10.1016/j.addma.2016.02.003
Gaynor AT, Guest JK (2016) Topology optimization considering overhang constraints: eliminating sacrificial support material in additive manufacturing through design. Struct Multidisc Optim 54(5):1157–1172. https://doi.org/10.1007/s00158-016-1551-x
Greifenstein J, Stingl M (2020) Topology optimization with worst-case handling of material uncertainties. Struct Multidisc Optim 61(4):1377–1397. https://doi.org/10.1007/s00158-019-02411-7
Gu DD, Meiners W, Wissenbach K, Poprawe R (2012) Laser additive manufacturing of metallic components: materials, processes and mechanisms. Int Mater Rev 57(3):133–164. https://doi.org/10.1179/1743280411Y.0000000014
Gu H, Behtash M, Hu Z, Hu C, Norato JA (2026) A geometry projection method for reliability-based topology optimization with dimensional and positional variability. Struct Multidisc Optim 69(2):33. https://doi.org/10.1007/s00158-025-04218-1
Holmberg E, Torstenfelt B, Klarbring A (2013) Stress constrained topology optimization. Struct Multidisc Optim 48:33–47. https://doi.org/10.1007/s00158-012-0880-7
Jaeger JC, Cook NG, Zimmerman R (2009) Fundamentals of rock mechanics. Wiley
Jansen M, Lombaert G, Diehl M, Lazarov BS, Sigmund O, Schevenels M (2013) Robust topology optimization accounting for misplacement of material. Struct Multidisc Optim 47:317–333. https://doi.org/10.1007/s00158-012-0835-z
Kan WH, Chiu LNS, Lim CVS, Zhu Y, Tian Y, Jiang D, Huang A (2022) A critical review on the effects of process-induced porosity on the mechanical properties of alloys fabricated by laser powder bed fusion. J Mater Sci 57(21):9818–9865. https://doi.org/10.1007/s10853-022-06990-7
Keshavarzzadeh V, James KA (2019) Robust multiphase topology optimization accounting for manufacturing uncertainty via stochastic collocation. Struct Multidisc Optim 60(6):2461–2476. https://doi.org/10.1007/s00158-019-02333-4
Keshavarzzadeh V, Fernandez F, Tortorelli DA (2017) Topology optimization under uncertainty via non-intrusive polynomial chaos expansion. Comput Methods Appl Mech Eng 318:120–147. https://doi.org/10.1016/j.cma.2017.01.019
Kim FH, Moylan SP (2018) Literature review of metal additive manufacturing defects. NIST Adv Manuf Ser. https://doi.org/10.6028/NIST.AMS.100-16
King WE, Barth HD, Castillo VM, Gallegos GF, Gibbs JW, Hahn DE, Kamath C, Rubenchik AM (2014) Observation of keyhole-mode laser melting in laser powder-bed fusion additive manufacturing. J Mater Process Technol 214(12):2915–2925. https://doi.org/10.1016/j.jmatprotec.2014.06.005
Kirsch EG (1898) Die Theorie der Elastizität und die Bedürfnisse der Festigkeitslehre, vol 42. Springer
Komini L, Langelaar M, Kriegesmann B (2023) Robust topology optimization considering part distortion and process variability in additive manufacturing. Adv Eng Softw 186:103551. https://doi.org/10.1016/j.advengsoft.2023.103551
Kriegesmann B, Lüdeker JK (2019) Robust compliance topology optimization using the first-order second-moment method. Struct Multidisc Optim 60:269–286. https://doi.org/10.1007/s00158-019-02216-8
Krüger JC, Kriegesmann B (2024) Robust design optimization using a non-intrusive second-order approximation of stochastic moments. Struct Multidisc Optim 67(7):124. https://doi.org/10.1007/s00158-024-03843-6
Langelaar M (2016) Topology optimization of 3d self-supporting structures for additive manufacturing. Addit Manuf 12:60–70. https://doi.org/10.1016/j.addma.2016.06.010
Langelaar M (2017) An additive manufacturing filter for topology optimization of print-ready designs. Struct Multidisc Optim 55(3):871–883. https://doi.org/10.1007/s00158-016-1522-2
Le C, Norato J, Bruns T, Ha C, Tortorelli D (2010) Stress-based topology optimization for continua. Struct Multidisc Optim 41:605–620. https://doi.org/10.1007/s00158-009-0440-y
Leung CLA, Marussi S, Atwood RC, Towrie M, Withers PJ, Lee PD (2018) In situ x-ray imaging of defect and molten pool dynamics in laser additive manufacturing. Nat Commun 9(1):1355. https://doi.org/10.1038/s41467-018-03734-7
Mahtabi M, Yadollahi A, Ataollahi S, Mahtabi MJ (2023) Effect of build height on structural integrity of Ti-6Al-4V fabricated via laser powder bed fusion. Eng Fail Anal 154:107691. https://doi.org/10.1016/j.engfailanal.2023.107691
Masuo H, Tanaka Y, Morokoshi S, Yagura H, Uchida T, Yamamoto Y, Murakami Y (2018) Influence of defects, surface roughness and HIP on the fatigue strength of Ti-6Al-4V manufactured by additive manufacturing. Int J Fatigue 117:163–179. https://doi.org/10.1016/j.ijfatigue.2018.07.020
Mommeyer C, Lombaert G, Schevenels M, Sigmund O (2024) Taylor series approximations for faster robust topology optimization. Struct Multidisc Optim 67(10):181. https://doi.org/10.1007/s00158-024-03890-z
Nayebi A, Rokhgireh H, Araghi M, Mohammadi M (2021) Modelling the asymmetric tension-compression properties of additively manufactured alloys using continuum damage mechanics. Proc Inst Mech Eng L 235(9):1969–1980. https://doi.org/10.1177/14644207211013434
Nejadseyfi O, Geijselaers H, van den Boogaard T (2019) Robust optimization based on analytical evaluation of uncertainty propagation. Eng Optim. https://doi.org/10.1080/0305215X.2018.1536752
Pilkey WD, Pilkey DF, Bi Z (2020) Peterson's stress concentration factors. Wiley
Rice JR, Tracey DM (1969) On the ductile enlargement of voids in triaxial stress fields. J Mech Phys Solids 17(3):201–217. https://doi.org/10.1016/0022-5096(69)90033-7
Sanaei N, Fatemi A, Phan N (2019) Defect characteristics and analysis of their variability in metal L-PBF additive manufacturing. Mater Des 182:108091. https://doi.org/10.1016/j.matdes.2019.108091
Schevenels M, Lazarov BS, Sigmund O (2011) Robust topology optimization accounting for spatially varying manufacturing errors. Comput Methods Appl Mech Eng 200(49–52):3613–3627. https://doi.org/10.1016/j.cma.2011.08.006
Schmidt T, Kriegesmann B, Seifried R (2024) Robust contact-constrained topology optimization considering uncertainty at the

contact support. Struct Multidisc Optim 67(4):46. https://doi.org/10.1007/s00158-024-03750-w

Seifi M, Salem A, Satko D, Shaffer J, Lewandowski JJ (2017) Defect distribution and microstructure heterogeneity effects on fracture resistance and fatigue behavior of EBM Ti-6Al-4V. Int J Fatigue 94:263–287. https://doi.org/10.1016/j.ijfatigue.2016.06.001

Sigmund O (2007) Morphology-based black and white filters for topology optimization. Struct Multidisc Optim 33(4):401–424. https://doi.org/10.1007/s00158-006-0087-x

Sigmund O (2009) Manufacturing tolerant topology optimization. Acta Mech Sin 25:227–239. https://doi.org/10.1007/s10409-009-0240-z

Snow Z, Nassar AR, Reutzel EW (2020) Invited review article: review of the formation and impact of flaws in powder bed fusion additive manufacturing. Addit Manuf 36:101457. https://doi.org/10.1016/j.addma.2020.101457

Svanberg K (1987) The method of moving asymptotes-a new method for structural optimization. Int J Numer Methods Eng 24(2):359–373. https://doi.org/10.1002/nme.1620240207

Tu J, Choi KK, Park YH (1999) A new study on reliability-based design optimization. J Mech Des 121:557–564. https://doi.org/10.1115/1.2829499

Wang F, Lazarov BS, Sigmund O (2011) On projection methods, convergence and robust formulations in topology optimization. Struct Multidisc Optim 43:767–784. https://doi.org/10.1007/s00158-010-0602-y

Wang S, Ning J, Zhu L, Yang Z, Yan W, Dun Y, Xue P, Xu P, Bose S, Bandyopadhyay A (2022a) Role of porosity defects in metal 3D printing: formation mechanisms, impacts on properties and mitigation strategies. Mater Today 59:133–160. https://doi.org/10.1016/j.mattod.2022.08.014

Wang W, Ning J, Liang SY (2022b) Analytical prediction of keyhole porosity in laser powder bed fusion. Int J Adv Manuf Technol 119(11): 6995–7002. https://doi.org/10.1007/s00170-021-08276-9

Yang RJ, Chen CJ (1996) Stress-based topology optimization. Struct Optim 12(2):98–105. https://doi.org/10.1007/BF01196941

Yavari R, Smoqi Z, Riensche A, Bevans B, Kobir H, Mendoza H, Song H, Cole K, Rao P (2021) Part-scale thermal simulation of laser powder bed fusion using graph theory: effect of thermal history on porosity, microstructure evolution, and recoater crash. Mater Des 204:109685. https://doi.org/10.1016/j.matdes.2021.109685

Publisher's Note Springer Nature remains neutral with regard to jurisdictional claims in published maps and institutional affiliations.